REPORT DOCUMENTATION PAGE

Form Approved OMB NO. 0704-0188

1. REPORT DATE (DD-MM-YYYY)	2. REPORT TYPE	3. DATES COVERED (From - To)
	Technical Report	-

4. TITLE AND SUBTITLE	5a. CONTRACT NUMBER
Year-two report.:--Silicon/Carbon Anodes with One-Dimensional Pore Structure for Lithium-Ion Batteries	W911NF-11-1-0231
	5b. GRANT NUMBER
	5c. PROGRAM ELEMENT NUMBER
	611102

6. AUTHORS	5d. PROJECT NUMBER
Yunhua Xu, Chunsheng Wang	
	5e. TASK NUMBER
	5f. WORK UNIT NUMBER

7. PERFORMING ORGANIZATION NAMES AND ADDRESSES	8. PERFORMING ORGANIZATION REPORT NUMBER
University of Maryland - College Park Research Administration 3112 Lee Building College Park, MD 20742 -5141	

9. SPONSORING/MONITORING AGENCY NAME(S) AND ADDRESS(ES)	10. SPONSOR/MONITOR'S ACRONYM(S)
U.S. Army Research Office P.O. Box 12211 Research Triangle Park, NC 27709-2211	ARO
	11. SPONSOR/MONITOR'S REPORT NUMBER(S)
	59134-CH.10

12. DISTRIBUTION AVAILIBILITY STATEMENT

Approved for public release; distribution is unlimited.

13. SUPPLEMENTARY NOTES

The views, opinions and/or findings contained in this report are those of the author(s) and should not contrued as an official Department of the Army position, policy or decision, unless so designated by other documentation.

14. ABSTRACT

In this report, we Si/C composite with porous and yolk-shell structure, carbon coated mesoporous Fe_2O_3, C/CuO and S/C composites using aerosol pyrolysis, electrospray and CVD techniques. The electrochemical peroformances of these materials were tested, and the mechanism for long cycling stability and high rate capability of these materials were investigated. The findings were published in top journals.

15. SUBJECT TERMS

Li-ion batteries, Na-ion batteries, Si/C anodes, S/C cathodes

16. SECURITY CLASSIFICATION OF:			17. LIMITATION OF ABSTRACT	15. NUMBER OF PAGES	19a. NAME OF RESPONSIBLE PERSON
a. REPORT	b. ABSTRACT	c. THIS PAGE			Chunsheng Wang
UU	UU	UU	UU		19b. TELEPHONE NUMBER
					301-405-0352

Report Title

Year-two report.:--Silicon/Carbon Anodes with One-Dimensional Pore Structure for Lithium-Ion Batteries

ABSTRACT

In this report, we Si/C composite with porous and yolk-shell structure, carbon coated mesoporous Fe2O3, C/CuO and S/C composites using aerosol pyrolysis, electrospray and CVD techniques. The electrochemical peroformances of these materials were tested, and the mechanism for long cycling stability and high rate capability of these materials were investigated. The findings were published in top journals.

Silicon/Carbon Anodes with One-Dimensional Pore Structure for Lithium-Ion Batteries

Grant # W911NF1110231

Annual Progress report

September 1 31, 2012 to August 31, 2013

Submitted by:

Chunsheng Wang, Ph.D.
Principal Investigator
Department of Chemical and Biomolecular Engineering
University of Maryland
College Park, Maryland 20740
Phone: 301-405-0352
cswang@umd.edu

Annual Reports (2011-2012)

1. <u>Objective</u>

The objectives of this project in the year-two are to develop porous Si/C and C/S composite electrodes for high performance lithium ion batteries and to investigate the mechanism how the porous carbon matrix enhances the cycling stability of Si and S electrodes.

2. <u>Summary of accomplishments in Year Two</u>

- ➤ Synthesis and characterization of self-assembled microsized porous Si/C particles by electrospray synthesis.
- ➤ Synthesis and characterization of yolk-shell structured Si/C composite anodes for lithium-ion batteries.
- ➤ Synthesis and characterization of C/Si composite anodes by in-situ polymer coating.
- ➤ Synthesis and characterization of mesoporous Fe_2O_3 and nano-structured carbon-coated CuO hollow spheres by aerosol pyrolysis spray as anodes for lithium-ion battereis.
- ➤ Synthesis and characterization of mesoporous C/S composite cathodes for room temperature sodium-ion batteries and lithium-ion batteries.

3. <u>Achievements</u>

- ➤ Yunhua Xu, Qing Liu, Yujie Zhu, Yihang Liu, Alex Langrock, Michael R. Zachariah, Chunsheng Wang, Uniform Nano-Sn/C Composite Anodes for Lithium Ion Batteries, *Nano Letters* 13, 470, 2013.
- ➤ Yonglin Liu,[§] Yunhua Xu,[§] Xiaogang Han, Chris Pellegrinelli, Yujie zhu, Hongli zhu, Jiayu Wan, Alex Chong Chung, Oeyvind Vaaland, Chunsheng Wang, Liangbing Hu, Porous Amorphous $FePO_4$ Nanoparticles Connected by Single-Wall Carbon Nanotubes for Sodium Ion Battery Cathodes, *Nano Letters* 12, 5664, 2012. ([§]equal contribution)
- ➤ Chao Luo,[§] Yunhua Xu,[§] Yujie Zhu, Yihang Liu, Shiyou Zheng, Ying Liu, Alex Langrock, Chunsheng Wang, Selenium@Mesoporous carbon composite with superior lithium and sodium storage capacity, *ACS Nano*, DOI: 10.1021/nn403108w. ([§]equal contribution)
- ➤ Yunhua Xu, Guoqiang Jian, Yihang Liu, Yujie Zhu, Michael R. Zachariah, Chunsheng Wang, Mesoporous Fe_2O_3 Spheres as Anodes for Lithium-Ion Battereis, submitted to *Nano Energy*.

4. <u>Details Accomplishments for Year-Two</u>

4.1 **Self-assembled microsized porous Si/C particles by electrospray**

Self-assembled microsized porous Si/C particles were fabricated by a one-step electrospray process, which is based on a process where a liquid jet breaks up under the influence of the

electrical force. The electrospray formation of microparticles is conceptually simple. Simply, silicon nanoparticles are dispersed into a polymer solution (e.g. PAN) and electrosprayed to form micro-droplets which are further dried after solvent removal.   The Si/polymer particles underwent calcinations at 600°C for 1 h in a tube furnace with flow Ar gas. Two polymers were employed in this study. One is polyacrylonitrile (PAN), soluble in DMF and showing a high carbon yield. Another is polyvinylpyrrolidone (PVP), soluble in ethanol and delivering a low carbon yield.

4.1.1 Synthesis and characterization of C/Si composite using PVP as a carbon source

The morphology and structure of the self-assembled microparticles were investigated using scanning electron microscopy (SEM, Hitachi SU-70, Japan) and transmission electron microscopy (TEM, JEOL 2100F, Japan) before and after calcination. Figure 1 shows the SEM and TEM images of self-assembled microparticles prepared from PVP/Si nanoparticles. Before calcination, the product shows random-shaped particles with diameter of ~ 5 um (Figure 1a and b). No Si nanoparticles were observed due to the large amount of polymer on the surface of the self-assembled particles. Interestingly, after calcination, spherical porous particles with size of about 4 um can be observed (Figure 1c-e). The porous structure was clearly demonstrated in the enlarged SEM image in Figure 1d and TEM image in Figure 1f. The high resolution SEM image in Figure 1e shows the carbonization of PVP produces where carbon granules distributed in the self-assembled microparticles with Si nanoparticles. The porous structure provides additional space to accommodate the huge volume change of Si nanoparticles during lithiation/delithiation reactions. The elastic carbon granules would benefit to release the strain led to by volume change and function as conductive agent.

4.1.2 Electrochemical performance of C/Si composite using PVP as a carbon source

The electrochemical performance of the self-assembled Si/C micropartices made from PVP was investigated in a coin-style half-cell using Li as a counter electrode. The self-assembled Si/C micropartices were mixed with carbon black and sodium Na-alginate binder to form slurry at the weight ratio of 80:10:10. The electrode was prepared by casting the slurry onto copper foil using a doctor blade and dried in a vacuum oven at 100°C overnight. Coin cells were assembled with lithium foil as the counter electrode, 1M $LiPF_6$ in a mixture of FEC/DMC (1:1 by volume) as the electrolyte, and Celgard®3501 (Celgard, LLC Corp., USA) as the separator. The cycling

3

performance was tested using Arbin battery test station (BT2000, Arbin Instruments, USA). Batteries were scanned between 0.02 – 1.5 V at the current density of 500 mA/g. Capacity was calculated on the basis of total mass of Si and carbon.
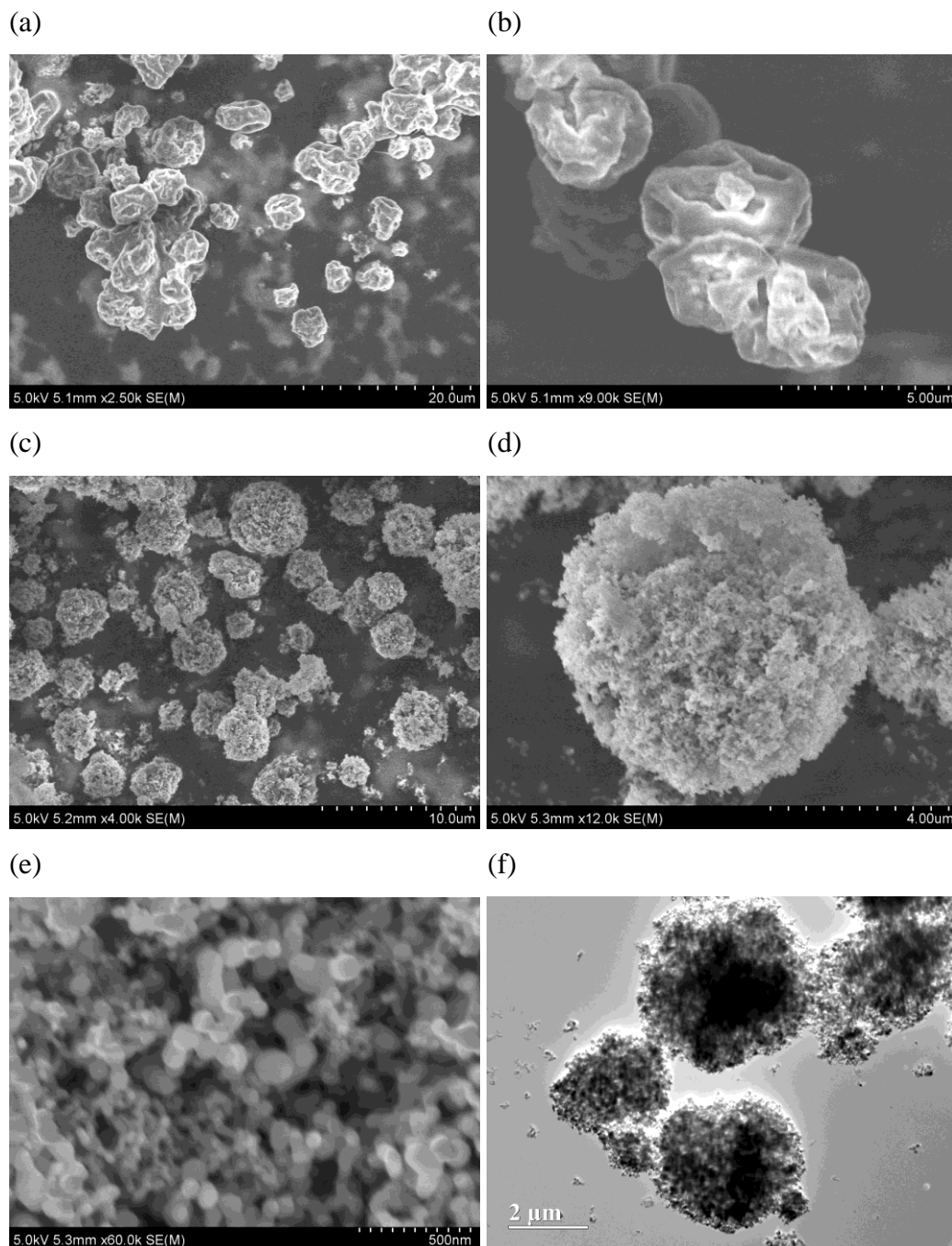
(a) (b)

(c) (d)

(e) (f)

Figure 1. SEM images of self-assembled microparticles (a, b) before and (c-e) after calcination. (f) TEM image of self-assembled microparticles after calcination. Polymer employed is PVP.

4

Figure 2 shows the electrochemical properties of the self-assembled Si/C micropartices. The reversible capacity is over 2000 mAh/g at the first cycle. The capacity of 1755 mAh/g was retained after 10 cycles. Figure 2b shows the Coulombic efficiency over the 10 cycles. For the first cycle, it delivered an efficiency of as high as 82.6%. Such high value is rare reported for Si-based anodes. In the following cycles, the efficiency remains a high level of >97%.
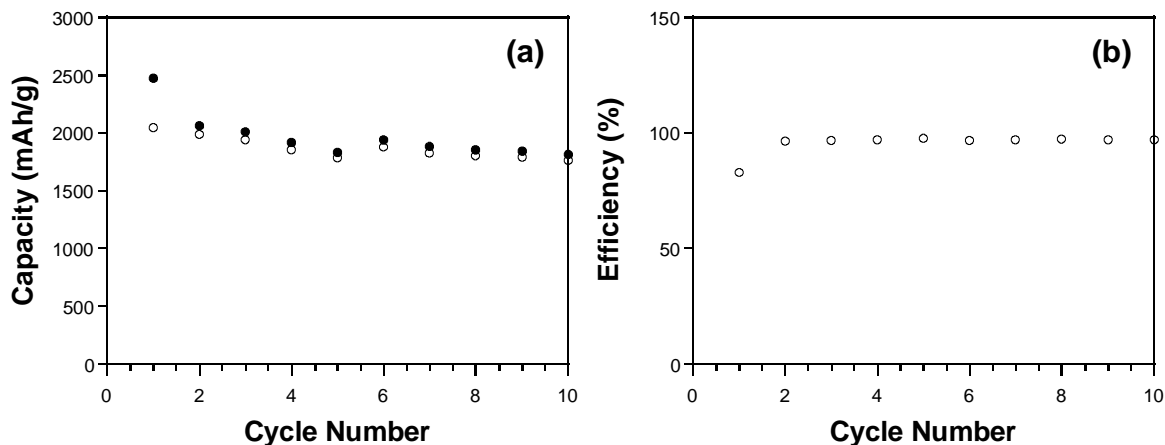

Figure 2. Cycling performance of the self-assembled Si/C microparticles.

4.1.3 Synthesis and characterization of C/Si composite using PAN as a carbon source

The Self-assembled microsized porous Si/C particles made with PAN were prepared at the same conditions. Si nanoparticles were dispersed in PAN/DMF solution and sprayed into microparticles. The Si/polymer particles underwent calcinations at 600°C for 1 h in a tube furnace with flow Ar gas. The carbon content in final products were estimated to be 15 wt% based on the weight loss before and after calcination.

The morphology and structure of the PAN-based self-assembled Si/C microparticles were investigated using the same techniques described above. Figure 3 shows the SEM and TEM images of the PAN-based self-assembled Si/C microparticles. Different from the PVP-based particles, self-assembly structure of Si nanoparticles can be clearly observed in the SEM images in Figure 3a and b before calcination. The enlarged SEM image in Figure 3b shows that PAN is uniformly coated on the surface of Si particles. After calcination, no obvious morphology changes were found, spherical shape and porous structure. Compared the SEM images before and after calcination, less coating was observed caused by the carbonization. The high resolution SEM image in Figure 3e also revealed that carbon was uniformly coated on the surface and

5

distributed in the microparticles, which ensures a good conductivity and mechanical integration. More dense packing structure was revealed by the TEM image in Figure 3f.
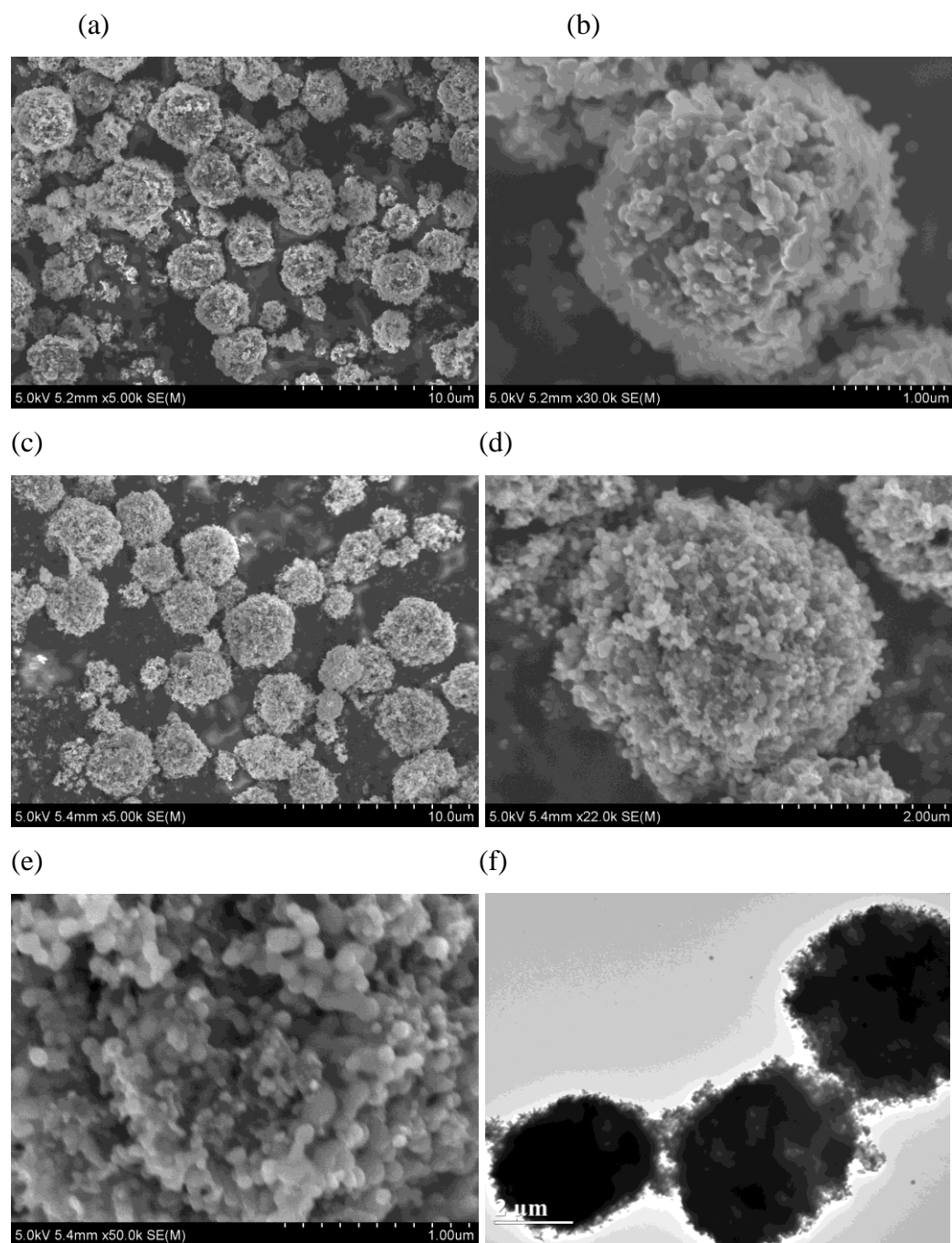
(a)

(b)

(c)

(d)

(e)

(f)

Figure 3. SEM images of the PAN-based self-assembled Si/C microparticles (a, b) before and (c-e) after calcination. (f) TEM image of the PAN-based self-assembled Si/C microparticles after calcination.

4.1.4Electrochemical performance of C/Si composite using PAN as a carbon source

The electrochemical performance of the PAN-based self-assembled Si/C microparticles was investigated in a coin-style half-cell using Li as the counter electrode. Cells were fabricated using the same procedures above. In this case, two electrolytes were employed. One is 1M $LiPF_6$ in a mixture of FEC/DMC (1:1 by volume) and another is 1M $LiPF_6$ in a mixture of EC/DEC (1:1 by volume). Cells was tested using Arbin battery test station (BT2000, Arbin Instruments, USA) at the current density of 500 mA/g between 0.02 − 1.5 V. Capacity was calculated on the basis of total mass of Si and carbon.
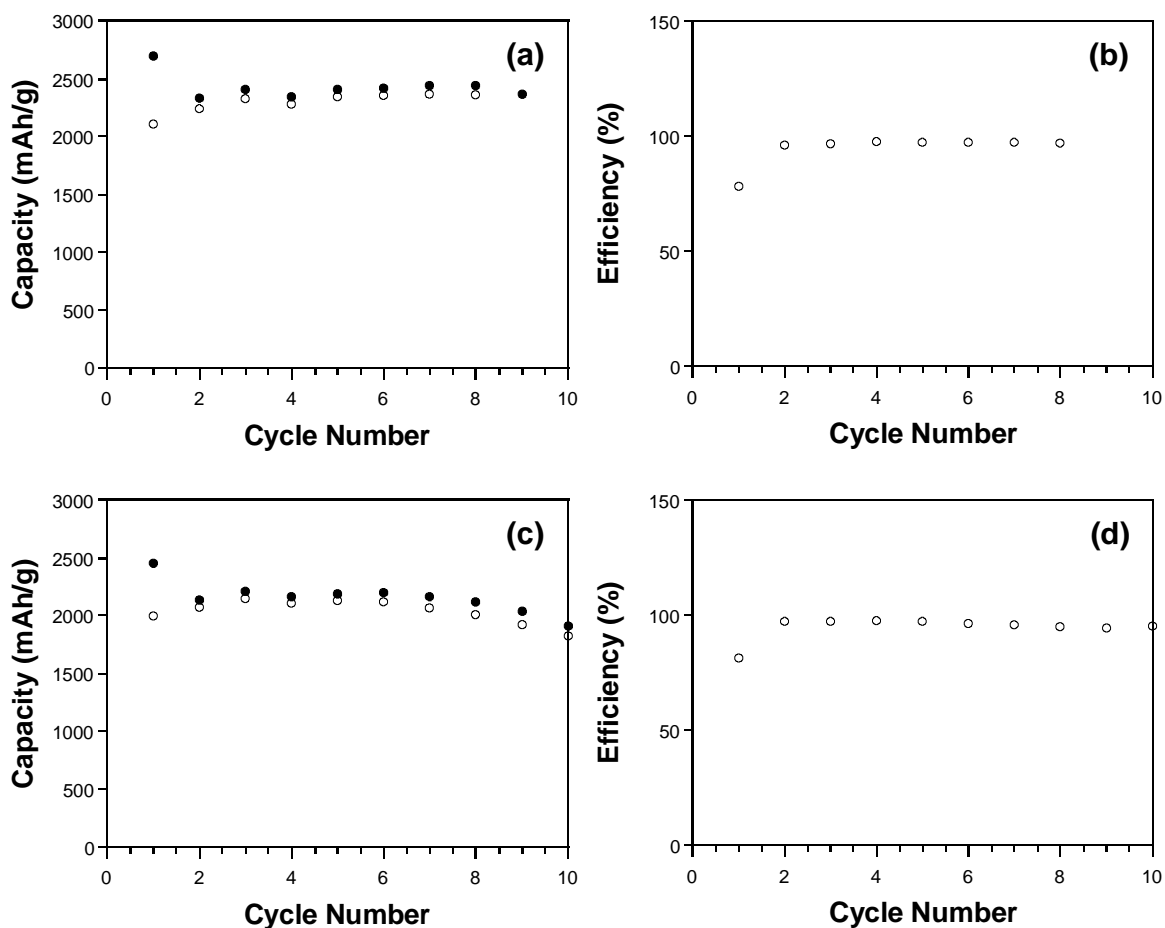

Figure 4. Cycling performance of the self-assembled Si/C microparticles. (a, b) used FEC/DMC electrolyte and (c, d) used EC/DEC electrolyte.

Figure 4 shows the electrochemical performance of the PAN-based self-assembled Si/C microparticles in 1M LiFP6 in FEC-SMC and 1M LiFP6 in EC-DMC two electrolytes. Reversible capacity of over 2000 mAh/g at the first cycle was obtained in both electrolytes. In particular, a capacity of over 2300 mAh/g was delivered for the FEC/DMC electrolyte, which is 6 times higher than the commercial graphite anodes. Although the FEC/DMC electrolyte displays a lower coulombic efficiency (78%) in the first cycle than the EC/DEC electrolyte (82%), better cycling stability were achieved for the FEC/DMC electrolyte with no capacity loss after 10 cycles. In comparison, the capacity decreases from 1994 mAh/g to 1820 mAh/g for the EC/DEC electrolyte after10 cycles. The exceptional performance makes the PAN-based self-assembled Si/C microparticles a promising anode for Li-ion batteries.

4.2 **yolk-shell structured Si/C anodes**

4.2.1 Synthesis and characterization of SiO$_2$@Si and carbon coated SiO$_2$@Si composites

SiO$_2$@Si composite. A sol-gel reaction was started by dispersing 100 mg commercial Si particles with average size of 100 nm in 50 ml ethanol using an ultrasonic bath (Aquasonic Model 75T, VWR Scientific Products). After ~5 min, a homogeneous yellowish suspension was formed. 3 ml concentrated NH$_4$OH solution (~28 wt%) was then added. The suspension was mixed for 30 min by mild stirring before adding any other reactants. A desired amount (typically 2.5 g) of tetraethyl orthosilicate (TEOS) was diluted with 10 ml ethanol in a 20 ml glass vial to form the SiO$_2$ precursor aolution. A syringe pump (Pump 11, Harvard Apparatus) was used to feed the SiO$_2$ precursor solution into the Si suspension at a rate of 1 ml/h. After addition of the SiO$_2$ precursor solution, the suspension became milky yellowish. Stirring was continued for 12 hours to compete the condensation reaction of SiO$_2$. Everything was carried out at room temperature. The product was collected by centrifugation at 7000 rpm for 5 min and washed by dispersing in absolute ethanol. The ethanol washing and centrifugation steps were repeated three times. A vacuum oven was utilized to dry the wet product at room temperature overnight.

Porous carbon coated SiO$_2$@Si composites. The coating of carbon shell on the prepared SiO$_2$@Si composites were prepared using similar processes to those of Yokoi et al. Furfuryl alcohol (Sigma-Aldrich, 98% purity) and oxalic acid (Sigma-Aldrich, 99+% purity) were used as the carbon source and acid catalyst, respectively, for the formation of the carbon shells. Typically, 100 mg of SiO$_2$@Si particles were mixed with a solution consisting of 50 mg of

furfuryl alcohol, 5 mg of oxalic acid, and 200 mg of ethanol by the incipient-wetness technique. The resulting product was vacuumed at room temperature for 1 hour and then heated to 343 K for 48 h to allow the polymerization of furfuryl alcohol, then placed in flowing N_2, first at 473 K for 3 h, to cure the polymer, and then heated at 1123 K for another 3 h to carbonize the polymer. The intermediate silica layer of $C@SiO_2@Si$ was dissolved in 10wt% HF solution (Aldrich, 30% purity) at room temperature for 10 min to yield the porous carbon coated Si nanoparticles. The as-obtained C@Si particles were collected by filtration followed by washing the particles with plenty of DI water to remove residue HF acid. The resulting product was vacuumed at room temperature overnight to dry the porous carbon coated Si particles.

Dense carbon coated C@Si composites. The coating of dense carbon layer on the C@Si composites was conducted as described above. Typically, 100 mg of $SiO_2@Si$ particles were mixed with a solution consisting of 100 mg of furfuryl alcohol, 5 mg of oxalic acid, and 150mg of ethanol by the incipient-wetness technique. The removal of ethanol, polymerization of furfuryl alcohol, and carbonization of the polymer were carried out in sequence to generate a dense layer of carbon on the porous carbon coated Si particles. The sample is ready for the electrochemical performance characterizations.

The structure of the yolk-shell structured Si/C anodes was examined by TEM (Figure 5). It is clearly revealed that Si nanoparticles were encapsulated within the spherical carbon shell. The carbon shell has a thickness of ~20 nm. This structure offers several advantages: first, the void provides large space to accommodate volume change during cycling processes. Second, carbon shell acts as mechanical layer to protect Si particles from pulverization and contact loss. Third, the carbon shell blocks the access of electrolyte to Si, and the new SEI formation caused by Si break can be prohibited. Therefore, good electrochemical performance is anticipated for the yolk-shell structured Si/C anodes.
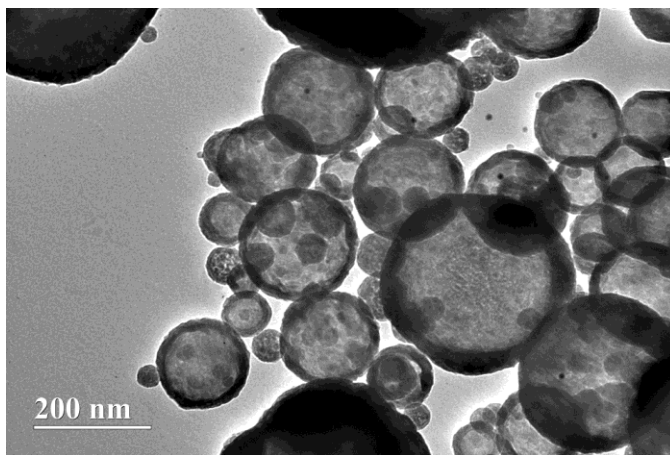

Figure 5. TEM images of the yolk-shell Si/C anode

4.2.2 Electrochemical performance

The yolk-shell Si/C anode was tested in a coin-style half cell using Li as the counter electrode. The yolk-shell Si/C particles were mixed with carbon black and sodium Na-alginate binder to form slurry at the weight ratio of 80:10:10. The electrode was prepared by casting the slurry onto copper foil using a doctor blade and dried in a vacuum oven at 100°C overnight. Coin cells were assembled with lithium foil as the counter electrode, were mixed with carbon black and sodium Na-alginate binder to form slurry at the weight ratio of 80:10:10. The electrode was prepared by casting the slurry onto copper foil using a doctor blade and dried in a vacuum oven at 100°C overnight. Coin cells were assembled with lithium foil as the counter electrode, 1M LiPF$_6$ in a mixture of ethylene carbonate/diethyl carbonate (EC/DEC, 1:1 by volume) and Celgard®3501 (Celgard, LLC Corp., USA) were used as electrolyte and separator, respectively. Electrochemical performance was tested using Arbin battery test station (BT2000, Arbin Instruments, USA). Batteries were scanned between 0.02 − 1.5 V at the current density of 500 mA/g. Capacity was calculated on the basis of total mass of the carbon and Si.

Figure 6 shows the electrochemical properties of the yolk-shell Si/C anode. The reversible capacity of 834 mAh/g was obtained in the first cycle and increased to about 900 mAh/g in the consequent cycles, which is two and half times higher than graphite anodes. In particular, excellent stability was demonstrated for the yolk-shell Si/C anode. After 30 cycles, a capacity of 938 mAh/g was delivered, which is even higher than the first cycle. The yolk-shell Si/C anode also shows a high efficiency of almost 100% except the first cycle, indicating a good reversibility. The good electrochemical performance is believed to benefit from the unique yolk-shell structure.
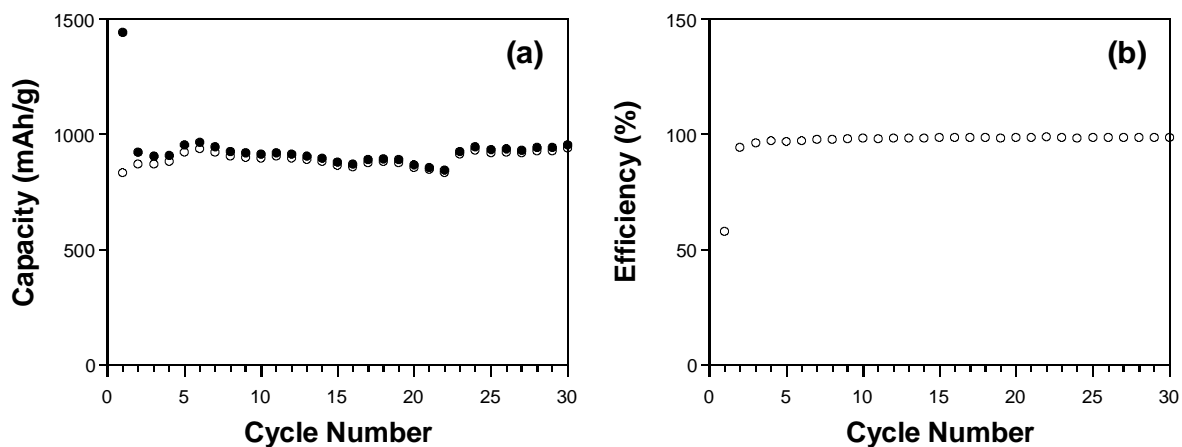

Figure 6. (a) Cycling performance and (b) charge/discharge profiles in the initial 2 cycles of the porous C/S composite.

10

4.3 **Carbon-coated Si nanoparticles by in-situ polymer coating**
4.3.1 Synthesis and characterization

Surface treatment of silicon nanoparticles. 2 g of silicon nanoparticles (average size ~50 nm) was carefully added to 100 mL of Piranha solution (H_2SO_4:H_2O_2, 70:30). Under the strong stirring, the solution was slowly heated up to 90 ^{o}C for 1 hr to oxidize the silicon surface. After cooled down to room temperature, the solution was poured into the large amount of diluted sodium carbonate solution to neutralize the sulfuric acid (*Caution, the intense heating for the solution*). The –OH functionalized silicon nanoparticles were then collected by centrifuge (8000 rpm for 10 min), and further washed twice with water and once with ethanol. The nanoparticles were dried at 40 ^{o}C overnight under vacuum.

Surface initiated ATRP. The silicon nanoparticles tethered with polymer were synthesized from surface initiated ATRP. Typical, CuCl(I) (120 mg, 1.2 mmol), Silicon nanoparticles (500 mg, mmol), PMDETA (540 µL, 2.4 mmol), and styrene (12 g, 120 mmol) were dissolved in 20 mL of THF in a 50 mL flask. The reaction mixture was degassed by three freeze-pump-thaw cycles and then filled with N2. The flask was placed in a preheated oil bath at 70 ^{o}C for 6 hr. After the polymerization, the reaction mixture was cooled to room temperature and diluted with THF. The polymer functionalized silicon nanoparticles were purified by centrifuge (8000 rpm for 15 min), and further washed with THF until the supernatant became colorless. The nanoparticles were dried overnight at 40 ^{o}C under vacuum.

The Carbon-coated Si nanoparticles were prepared by in-situ polymer coating followed by carbonization at 700C in argon gas. The composite structure was examined by SEM, shown in Figure 7. It is found that Si nanoparticles are uniformed coated with carbon. The uniform coating of carbon not only offers a mechanical support to release the stress/strain caused by lithium ion insertion/extraction during electrochemical cycling and thus protect Si particles from pulverization, but also provides a pathway to electrons and lithium ions to improve the conductivity.
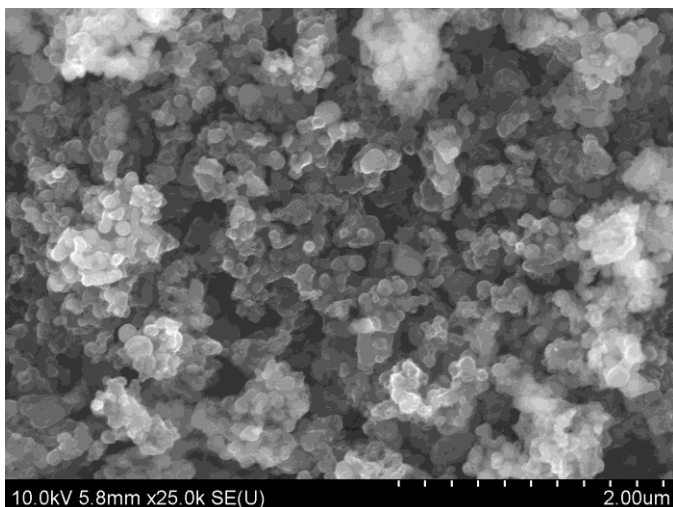
Figure 7. SEM image of the carbon-coated Si nanoparticles.

4.3.2 Electrochemical performance

Electrochemical performance of the carbon-coated Si nanoparticles was evaluated in two-electrode coin cells using lithium as the counter electrode. The carbon-coated Si nanoparticles were mixed with carbon black and sodium-alginate binder to form slurry at the weight ratio of 70:15:15. The electrode was prepared by casting the slurry onto copper foil using a doctor blade and dried in a vacuum oven at 100°C overnight. Coin cells were assembled with lithium foil as the counter electrode, 1M $LiPF_6$ in a mixture of FEC/DMC (1:1 by volume) as the electrolyte, and Celgard®3501 (Celgard, LLC Corp., USA) as the separator. Electrochemical performance was tested using Arbin battery test station (BT2000, Arbin Instruments, USA). Batteries were scanned between 0.02 – 1.5 V at the current density of 200 mA/g. Capacity was calculated on the basis of total weight of Si and carbon.

Figure 8 shows the cycling stability of the carbon-coated Si nanoparticles. The reversible capacity of 783 mAh/g was delivered in the first cycle, which is more than two times graphite. Most importantly, super stable cycling performance was presented for the carbon-coated Si nanoparticles. After 100 cycles, the capacity retention is still as high as 766 mAh/g (Figure 8a), corresponding to 98% of the first cycle. This means that the capacity loss is only 0.02% for each cycle. In the same time, coulombic efficiency close to 100% was obtained except the initial several cycles (Figure 8b), demonstrating a highly reversible electrochemical activity. These results show that the carbon-coated Si nanoparticles by in-situ polymer coating is a promising anode materials for lithium-ion batteries.
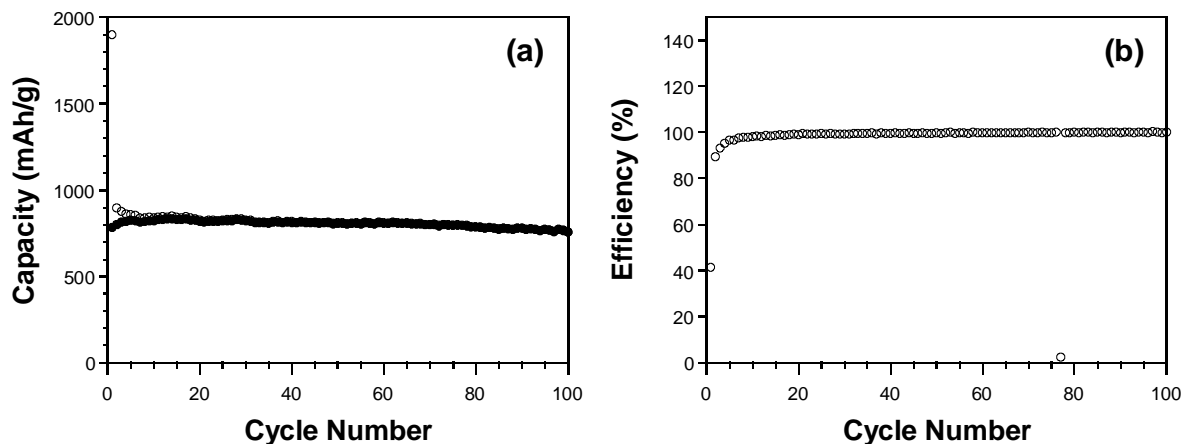
12

Figure 8. Electrochemical cycling performance of the carbon-coated Si nanoparticles.

4.4 Mesoporous Fe_2O_3 spheres by aerosol pyrolysis spray as anodes for lithium-ion battereis

4.4.1 Synthesis of Mesoporous Fe_2O_3 particles

Mesoporous Fe_2O_3 particles were prepared by an aerosol spray pyrolysis method as illustrated in Figure 9. Typically, ~3.2 g iron(III) nitrate nonahydrate ($Fe(NO_3)_3 \cdot 9H_2O$, Sigma-Aldrich) and 0.34 g sucrose ($C_{12}H_{22}O_{11}$, Sigma-Aldrich) were dissolved into 110 ml water. Aerosol droplets containing the dissolved precursors were generated using compressed air at a pressure of 0.24 MPa in a collision type atomizer. The geometric mean diameter of the droplets was measured to be ~1 μm by a laser aerosol spectrometer. The produced aerosol droplets were firstly passed through a silica-gel diffusion dryer to remove most of the water, and then passed to a tube furnace at 600 or 800°C. The normal residence time in the synthesis was around 1 second for a total gas flow rate of 3.5 L.min^{-1}.The final products were collected on a 0.4 μm (pore size) HTTP Millipore filter.
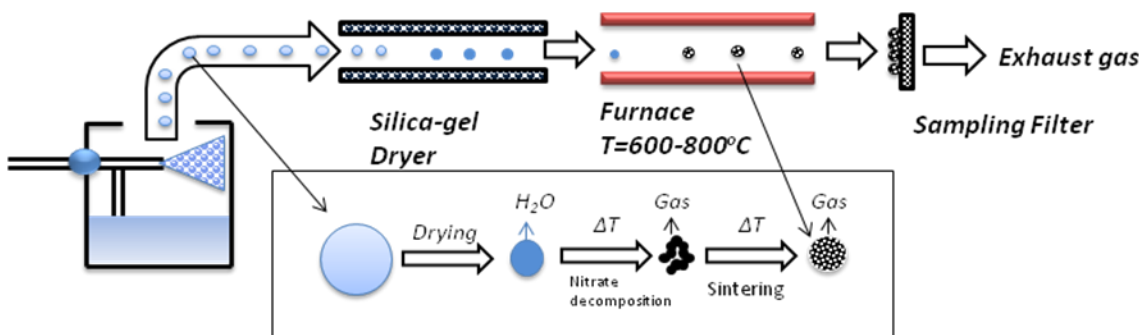

Figure 9. Illustration of aerosol spray pyrolysis route to mesoporous Fe_2O_3.

4.4.2 Material Characterizations

The morphology of Fe_2O_3 spheres was illustrated in the SEM images in Figure 10. Spherical shape of the precursor droplets was well preserved for both samples of Fe_2O_3-600 and Fe_2O_3-800, which is the typical feature of aerosol spray pyrolysis. The Fe_2O_3 spherical particles for both samples are distributed in the diameter range of hundreds of nanometers. The enlarged SEM image in Figure 10c clearly reveals the porous structure of cavities on the surface of the Fe_2O_3 spherical particles. The pores with nanometer size are uniformly distributed on the surface, implying a porous structure exists through the whole particles.
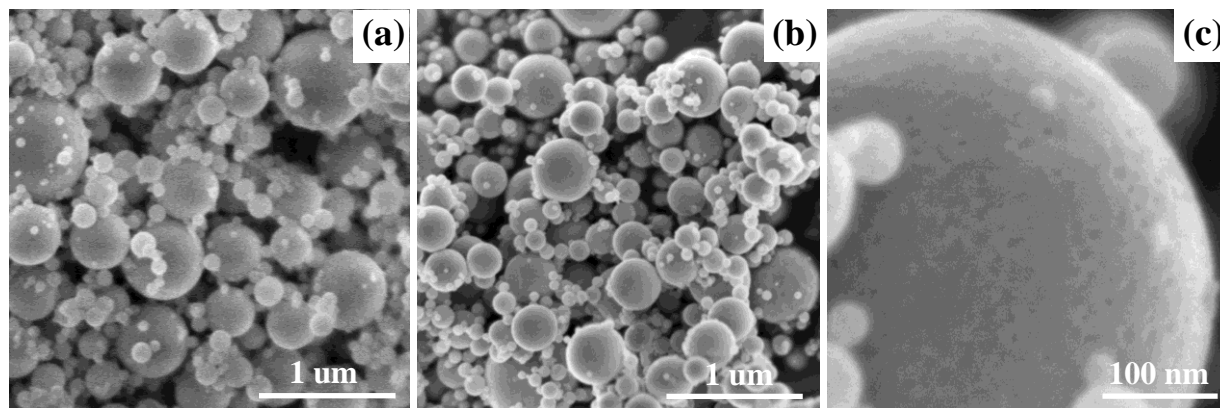

Figure 10. SEM images of Fe2O3 synthesized at (a) 600 C and (b, c) at 800 C.

The mesoporous nature inside the Fe_2O_3 spheres is evidenced by TEM images in Figure 11. For both samples of Fe_2O_3-600 and Fe_2O_3-800, the porous structure is clearly revealed with the contrast between Fe_2O_3 walls and mesopores in the TEM images. The lighter color represents pores, while the dark color represents Fe_2O_3 walls. Both the diameter of pores and the thickness of the Fe_2O_3 walls are in the range of a couple of nanometers. It is noted that Fe_2O_3-800 shows much higher contrast and better-defined pore structure than Fe_2O_3-600, which is attributed to the stronger thermal effects. At higher temperature, much faster and complete decomposition of the precursors occurred, facilitating formation of better crystal structure and leading to better-defined pores. The high resolution images clearly reveal a good crystal structure for Fe_2O_3-800 (Figure 12g); while an amorphous nature was displayed for Fe_2O_3-600 (Figure 11c). At lower temperature, short residence time in the reaction furnace is not enough to create fine crystal. This is further confirmed by the selected area electron diffraction (SAED) images (Figure 11d and h). Bright diffraction rings are presented for Fe_2O_3-800 (Figure 11h), which is typical feature of

crystal structure. However, only broad diffraction rings are observed for Fe_2O_3-600, indicating the amorphous structure.
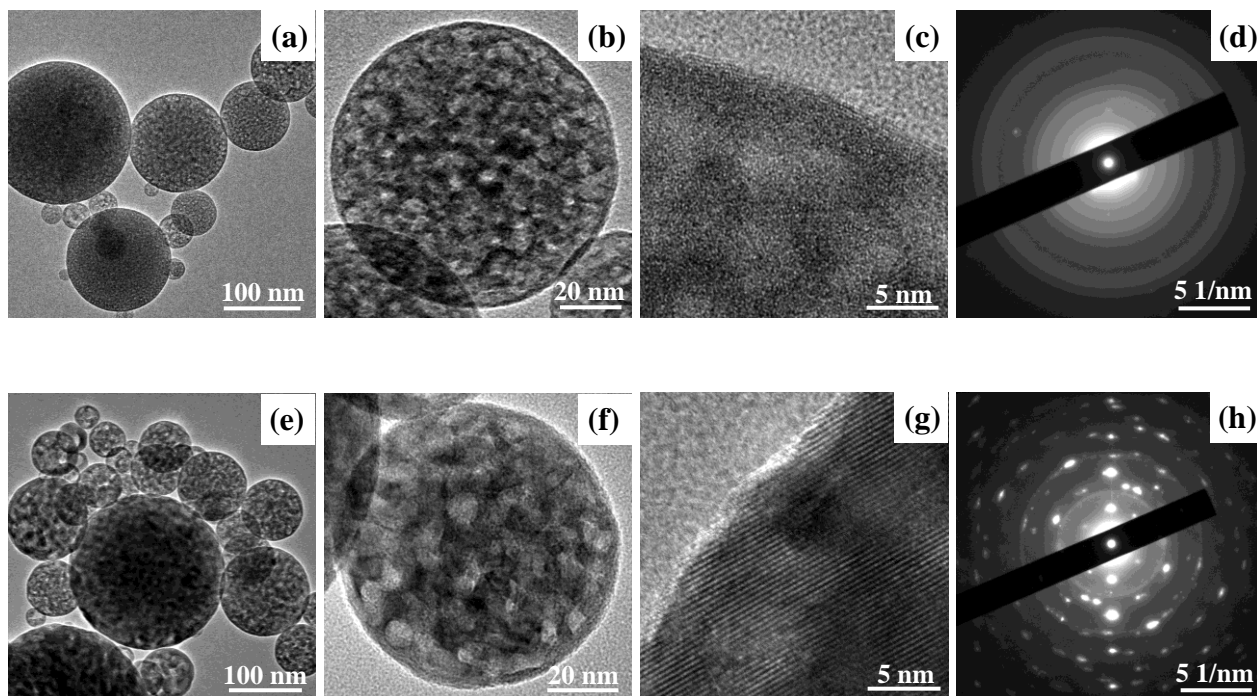

Figure 11. TEM images of Fe2O3 synthesized at (a-c) 600 C and (e-g) 800 C. SAED images of (d) Fe2O3-600 and (h) Fe2O3-800.

X-ray diffraction (XRD) analysis was performed on both Fe_2O_3-600 and Fe_2O_3-800, shown in Figure 12. Fine diffraction peaks were displayed for Fe_2O_3-800, which can be well indexed to the crystal structure of Fe_2O_3 (JCPDS card No.: 33-0664). No impurity peaks were observed, indicating that the thermal decomposition is complete and the synthesis temperature (800 C) is sufficient to form crystal Fe_2O_3 even the heating time is as short as several seconds. In contrast, no diffraction peaks are displayed for Fe_2O_3-600, which is in good agreement with the high-resolution TEM and SAED results (Figure 11c, d, g and h). The composition of Fe_2O_3 in Fe_2O_3-600 was evidenced by the charge/discharge profiles, revealing that the thermal decomposition to Fe_2O_3 occurred.
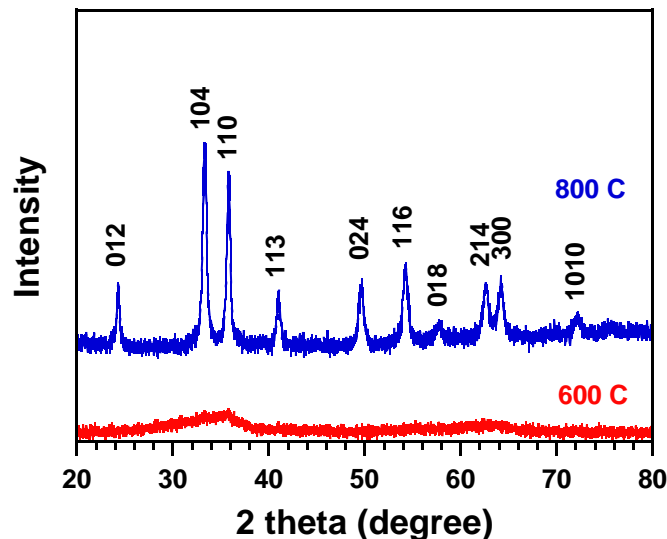
Figure 12. XRD pattern of Fe2O3 synthesized at 600 C and 800 C. 050637

The porous properties of the Fe_2O_3-800 spheres were analyzed using nitrogen absorption measurement. Figure 13 shows the adsorption isotherm. The Brunauer-Emmett-Teller (BET) specific surface area and pore volume are 23 m^2/g and 0.015 cm^3/g for Fe_2O_3-600, 58 m^2/g and 0.15 cm^3/g for Fe_2O_3-800, respectively. The surface area is much larger than those solid particles in literature. The high specific surface area of Fe_2O_3-800 provides large contact area between Fe_2O_3 and electrolyte. Combining the thin walls (a couple of nanometers) with short transport distance of ions, the porous structure ensures good electrochemical kinetics. In the meanwhile, the pores inside the Fe_2O_3 spherical particles offer extra void space to alleviate strain and accommodate volume changes. BJH average pore diameter is 10 nm and 11 nm for Fe_2O_3-600 and Fe_2O_3-800, respectively, which are in consistence with the results by TEM images.
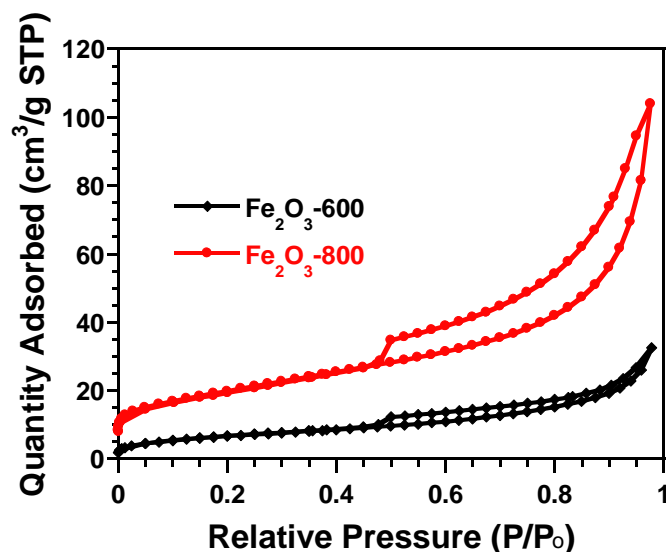
16

Figure 13. N_2 adsorption/desorption isotherm of mesoporous Fe_2O_3 anodes.

4.4.3 Electrochemical Measurements

Electrochemical performance of both Fe_2O_3-600 and Fe_2O_3-800 electrodes was investigated in coin cells using lithium as the counter electrode. Figure 14a and b show the cyclic voltammograms of the initial 2 cycles at a scan rate of 0.1 mV/s between 0 V and 3 V for both electrodes of Fe_2O_3-600 and Fe_2O_3-800. Strong reduction peaks at 0.65 V and 0.7 V were observed in the first cycle for Fe_2O_3-800 and Fe_2O_3-600, which is attributed to the conversion reaction of lithium ion insertion with the reduction from Fe^{3+} to Fe^0. In the second cycle, they moved to higher voltage of 0.9 V for Fe_2O_3-800 and 0.8 V for Fe_2O_3-600 with lower peak intensity. The peak position shift implies an irreversible phase transform in the first lithium ion insertion, which is a common observation for iron oxide anode materials in lithium-ion batteries.[15-34] The difference in the peak intensity mainly resulted from the decomposition of electrolyte to form solid-electrolyte interface (SEI) films. There is a small irreversible reduction peak appeared in the first cycle for Fe_2O_3-600 but disappeared in the second cycle, which is believed to be associated with the amorphous structure of Fe_2O_3-600. But it's absent for Fe_2O_3-800. Further, we noted that Fe_2O_3-800 has a larger peak voltage shift of 0.25 V between the first and second cycles compared to 0.1 V for Fe_2O_3-600, which is also related to their crystal and amorphous natures. In the anodic process, similar oxidation curves and peak intensity were

17

presented for both Fe_2O_3-600 and Fe_2O_3-800 in the first cycle with two broad peaks centered at 1.65 V and 1.85 V, respectively, accounting for the oxidation reaction of Fe^0 to Fe^{3+}. In the meanwhile, there is no significant difference was observed between the first and second cycles for both electrodes, demonstrating good reversibility of the porous Fe_2O_3 spherical particles. Corresponding to the small reduction peak of Fe_2O_3-600 in the first cycle, the first oxidation shows a broad wave at 0.5 V but disappeared in the second cycle. The similar CV curves between Fe_2O_3-600 and Fe_2O_3-800 in the second cycle revealed that the same conversion reaction occurred during lithium ion insertion and extraction, suggesting that Fe_2O_3 was successfully synthesized at both spray pyrolysis temperatures of 600 C and 800 C.
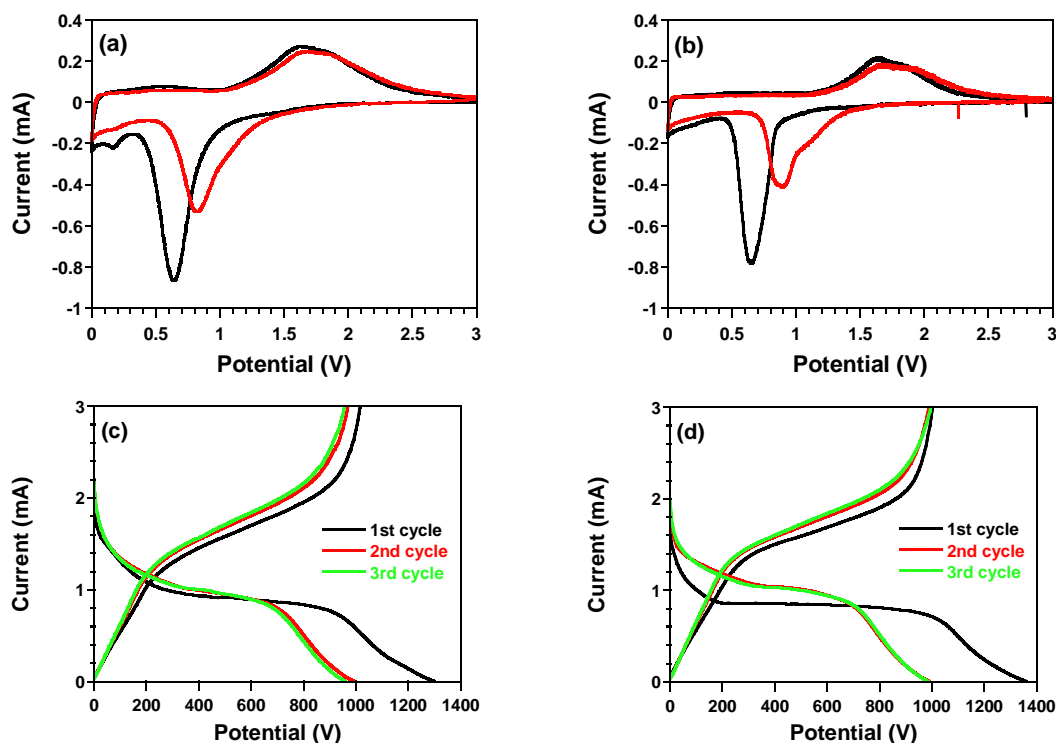

Figure 14. (a,b) Cyclic voltammograms of the initial 2 cycles scanned between 0 – 3 V at a rate of 0.1 mV/s, (c,d) charge/discharge profiles at the initial three cycles at 100 mA/g and 0 – 3 V for (a,c) Fe2O3-600 and (b,d) Fe2O3-800.

More information on the difference in electrochemical reactions between Fe_2O_3-600 and Fe_2O_3-800 can be found in the comparison of charge/discharge profiles. Figure 14c and d illustrated the first three charge/discharge curves of Fe_2O_3-600 and Fe_2O_3-800 at 100 mA/g and 0 – 3 V. Fe_2O_3-800 exhibits a rapid voltage decrease and reaches a long plateau at 0.8 V in the first discharge (Figure 14d), corresponding to the conversion reaction between Fe_2O_3 and lithium and

the irreversible decomposition reaction of electrolyte. In the following cycles, a slope between 1 – 1.5 V was observed, accounting for the reduction reaction of Fe^{3+} to Fe^0. The same results have been widely reported in literature and were attributed to the structure changes during the lithium insertion in the first cycle,[7,14] which irreversibly converts Fe_2O_3 to Fe and Li2O nano-grains and altered the crystal structure to an amorphous-like feature. There is no obvious difference in the charge process for the three cycles. They all show a slope at 1.5 – 2.5 V, representing the oxidation from Fe^0 to Fe^{3+}. The identical charge/discharge behaviors from the second cycle demonstrate a good reversibility and stability. In contrast, Fe_2O_3-600 presents a long slope before reaching a short plateau at ~ 0.9 V (Figure 14c). The amorphous nature of Fe_2O_3-600 is a determine factor for the slope shape in the first discharge process. As well known, slope voltage profile is a typical feature for amorphous electrode materials.[56,57] Similar to Fe_2O_3-800, the following cycles only show a slope at 1 – 1.5 V. Also similar charge profiles were displayed in the initial three cycles for Fe_2O_3-600.

The first discharge of Fe_2O_3-800 delivered a capacity of 1365 mAh/g, much higher than theoretical value of 1006 mAh/g. The extra capacity is attributed to the decomposition reaction of electrolyte. The reversible capacity of Fe_2O_3-800 in the first cycle is 1003 mAh/g, corresponding to 99.7% of the theoretical capacity. The high reversible capacity identifies full utilization of the porous Fe_2O_3 through the whole spherical particles. No capacity fading occurred in the following cycles, revealing good stability. Fe_2O_3-600 also delivered charge and discharge capacities of 1015 mAh/g and 1306 mAh/g, respectively, similar to those of Fe_2O_3-800, thus revealing the same high reversibility and reactivity as Fe_2O_3-800. However, large charge capacity loss was found in the following cycles, 45 mAh/g in the second cycle and 13 mAh/g in the third cycle. Despite similar reversible capacity was delivered in the first cycle for both Fe_2O_3-600 and Fe_2O_3-800, the large capacity decrease is an indicator of a worse stability for Fe_2O_3-600.

The cycling stability of the porous Fe_2O_3 electrodes was investigated by repeated charge/discharge processes between 0 and 3.0 V at the current density of 500 mA/g. For comparison, commercial Fe_2O_3 nanoparticles were also examined at the same test conditions. Data of the delithiation capacity are shown in Figure 15a. Fe_2O_3-800 provides a charge capacity of around 1000 mAh/g in the first cycle follow by slight capacity decay for 15 cycles and then remains unchanged at ~ 800 mAh/g up to 100 cycles. Unlike that the similar reversible capacity

were observed for both Fe_2O_3-600 and Fe_2O_3-800 at low current density of 100 mA/g, a lower capacity of 850 mAh/g was observed for Fe_2O_3-600 in the first cycle with fast capacity fading in the subsequent cycles. After 100 cycles, a capacity of 380 mAh/g was retained, which account for less than half of the initial cycle. The most fast capacity loss was observed for the commercial Fe_2O_3 nanoparticles. Although similar capacity was provided by the commercial nanoparticles in the initial cycles, they suffered a rapid capacity fading and failed to delivery capacity after 50 cycles. This clearly demonstrates that the superior cycling performance for the porous Fe_2O_3 synthesized using aerosol spray pyrolysis over the commercial nanoparticles. The fact of the better performance of Fe_2O_3-800 than Fe_2O_3-600 shows that crystal structure seems to be more promising than amorphous structure. The reason is probably crystal structure has a higher mechanical strength than amorphous structure. The former one would facilitate to alleviate the stress and strain caused by lithium insertion/extraction, and thus providing a strong mechanical support to keep the spherical particles in integration and thus improve the stability.
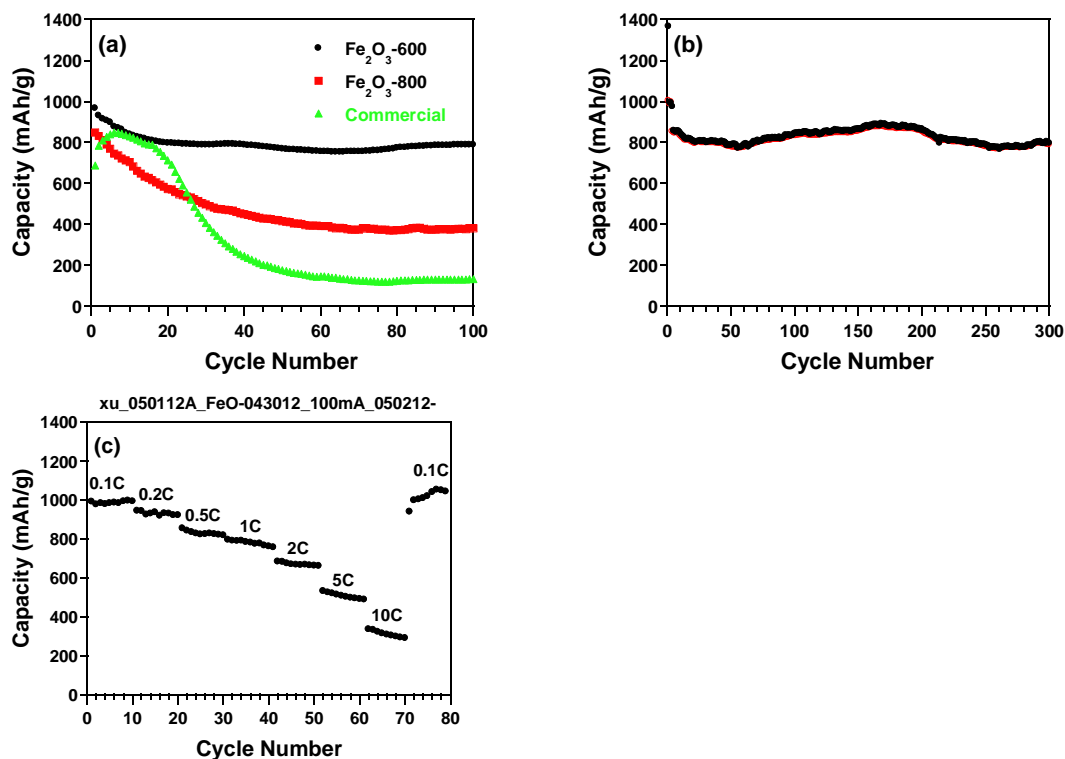

Figure 15. (a) Comparison of cycling performance of Fe2O3-600, Fe2O3-800 and commercial Fe2O3 particles. (b) Cycling performance of Fe2O3-800 at 500 mA/g and 0 – 3 V after three cycles at 100 mA/g. (c) Rate capability of Fe2O3-800.

The extended cycling behavior of Fe_2O_3-800 was further evaluated by cycling the electrode at 500 mA/g after three cycles at 100 mA/g, shown in Figure 15b. The exceptional stability was displayed. After 300 cycles, no capacity fading occurred with capacity retention of ~ 800 mAh/g. Such long-life cycling performance has barely been reported in literature although similar capacity has been realized by quite a few groups previously.[15,19,20,26,] This definitely proves that the mesoporous Fe_2O_3 sphere electrode synthesized at 800 C is a promising material for energy storage and rechargeable batteries.

The rate capability of the mesoporous Fe_2O_3-800 anodes was examined at different current densities. Excellent rate performance of the mesoporous Fe_2O_3-800 anodes was demonstrated in Figure 15c. A high capacity of 300 mAh/g was retained at a 10 C rate (C rate = 1006 mA/g), which is comparable to graphite used for commercial lithium ion batteries. Even at a higher rate of 20 C, the capacity retention is still as high as 120 mAh/g, which is much better than those previously reported solid iron oxide nanoparticles.[18] Remarkably, the rate capability of the mesoporous Fe_2O_3-800 anodes is superior to that of those conductive additive-incorporated iron oxide anodes, such as amorphous carbon, graphene as well as carbon nanotubes.[16,24,58-61] The excellent rate capability is believed to be associated with the mesoporous structure.

Clearly, the unique porous spherical structure of the mesoporous Fe_2O_3 anodes is responsible for the enhanced electrochemical performance. As well known, the porous structure provides extra space to accommodate the large volume change during lithium ion insertion/extraction, which helps alleviate the absolute strain on the surface and avoid mechanical crack, which maintains the integrity of the whole particle and good electric pass within the spherical particles, and thus improving the cycling stability and rate performance. In addition, the reduced dimension of Fe_2O_3 electrode (nano-sized walls) not only offers further assistance to reduce the strain led by lithiation/delithiation reaction, but also provides short transport distance for lithium ions and electrons, allowing fast kinetics. Large surface area of the porous Fe_2O_3 anodes offers a high electrolyte/electrode contact area, ensuring a fast charge transfer reaction on the surface. Along with the nano-sized dimension, this porous spherical structure enables an excellent rate capability. Finally, compared amorphous structure, the crystal structure is another factor to provide a strong mechanical support. As a result, the mesoporous crystal Fe_2O_3 spheres not only are able to fully utilize the Sn nanoparticles to store lithium ions, thus providing high capacity, but also improve the cycling stability and rate capability.

21

The material structure of the mesoporous Fe_2O_3 anodes after 100 charge/discharge cycles between 0 and 3.0 V at 500 mA/g current were investigated using TEM (Figure 16). The spherical shape of the mesoporous spheres was well sustained as a whole integration structure for both Fe_2O_3-600 than Fe_2O_3-800. High resolution TEM images (Figure 16b and e) revealed that the porous structure also survived the lithium ion insertion/extraction reactions for both anodes. In comparison to the porous structure with a wall-frame network of the fresh Fe_2O_3 spherical particles in Figure 11, the Fe_2O_3 spheres were converted to nanoparticle-assembly structure. The diameter of nanoparticles is around 10 nm. The conversion in porous structure is believed to be caused by the repeated lithiation/delithiation behavior. There is no doubt that the well-preserved morphology and porous structure of the mesoporous Fe_2O_3 anodes after 100 cycles prove that the mesoporous Fe_2O_3 spheres can effectively accommodate the volume change and alleviate the strain during the electrochemical cycles.
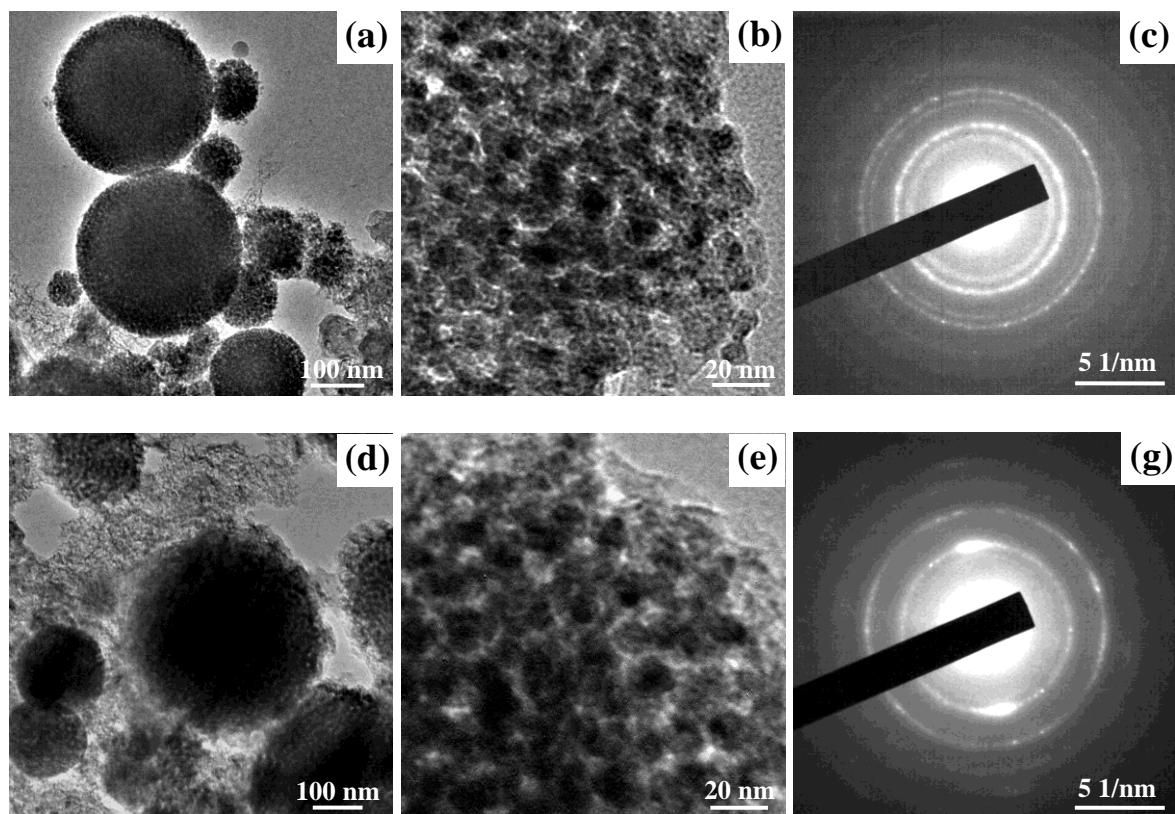

Figure 16. (a,b and d,e) TEM and (c,f) SAED images of Fe2O3 synthesized at (a-c) 600 C and (d-f) 800 C after 100 cycles.

The SAED was performed on Fe_2O_3 particles after 100 cycles. The images are shown in Figure 16c and f. Surprisingly, crystal pattern was displayed for both Fe2O3-600 than Fe2O3-800 anodes. This means that the amorphous feature of Fe2O3-600 was transformed to crystal structure. The worse cycling stability of Fe2O3-600 then Fe2O3-800 suggests that crystal materials are preferred for better battery performance.

In conclusion, mesoporous Fe_2O_3 spherical particles were synthesized at different temperatures of 600 C and 800 C using aerosol spray pyrolysis as anode material for lithium-ion batteries. Fe_2O_3-600 is amorphous, while Fe_2O_3-800 has a fine crystal structure. High capacity, good cycling stability as well as excellent rate capability were demonstrated for Fe_2O_3-800. The TEM results revealed that the electrochemical cycles converted the wall-frame porous structure into nanoparticle-assembly structure and transformed amorphous Fe_2O_3-600 into crystal feature. The better stability of Fe_2O_3-800 suggests that crystal structure is preferred for high performance Fe_2O_3 anode materials in LIBs. Our study not only provides a simple synthesis method for lithium ion batteries, but also helps in designing novel and high performance electrode materials.

4.5   Mesoporous C/S composite cathodes for room temperature sodium-ion batteries

4.5.1 Synthesis and characterization of sulfur/porous carbon.

Mesoporous carbon was prepared from sucrose. The resulting mesoporous carbon has been reported to have small pores and large pore volume. In addition, along with the high conductivity and good mechanical property of the porous carbon, these features make it a suitable host material for sulfur. In our study, sulfur was impregnated into the mesoporous carbon with a vapor-infusion method developed by our group. Sulfur was mixed with porous carbon and sealed in glass tubes under vacuum. The tubes underwent heat treatment at 600^oC to infuse sulfur into the mesoporous carbon. At this temperature, sulfur is in a gas state and was impregnated into porous carbon when cooling down. This method has been shown to be an efficient way to synthesize S/C composite electrode materials for lithium ion batteries.

SEM and TEM images of the porous C/S composites in Figure 17a and b show that the C/S composites have a spherical shape with a particle size of about 500 nm. The elemental mapping images in Figure 1c and d reveal that sulfur is homogenously distributed in the porous carbon spheres and no sulfur accumulation on the surface was observed, demonstrating a perfect sulfur infiltration into the mesoporous carbon. The sulfur impregnation was also confirmed by the

drastic decrease in specific surface area before (357 m^2/g) and after (7.5 m^2/g) sulfur infusion (Figure 18). The good conductivity and uniform distribution of sulfur in the porous carbon ensures a high utilization of sulfur and good rate capability during electrochemical reactions. The selected area electr7on diffraction (SAED) pattern (Figure 17e) shows only broad diffraction rings, indicating that no crystalline sulfur exists in the composite. This is confirmed by XRD analysis (shown in Figure 17f). Unlike the pristine sulfur, which shows characteristic diffraction peaks of the crystalline structure, the porous C/S composite displays the same shape as the porous carbon, indicating that very small sulfur was confined in the porous carbon.
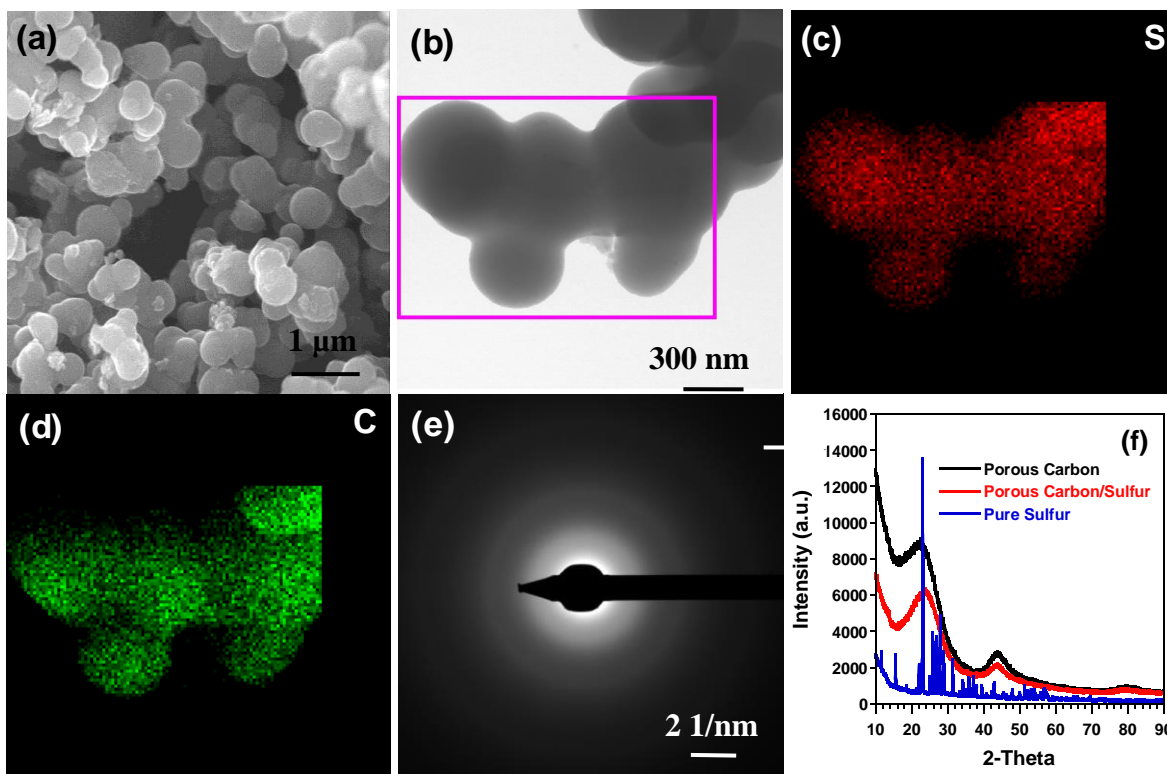

Figure 17. (a) SEM and (b) TEM image of the porous C/S composite. (c) and (d) Elemental mapping images of S and C for the marked region in (a). (e) SAED image of the porous C/S composite. (f) XRD curves of porous carbon, pristine sulfur and the porous C/S composite.
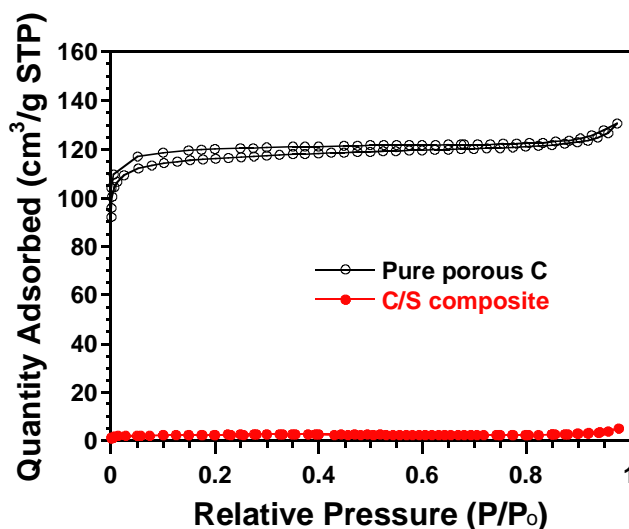
Figure 18. N$_2$ adsorption/desorption isotherm of pure porous C and C/S composite.

The nature of sulfur in the mesoporous carbon, the C/S composites, pure porous carbon and pristine sulfur were investigated with Raman. Data are shown in Figure 19. Typical Raman spectrum pattern of pristine sulfur is presented in Figure 19. Previous studies have shown that the stretching bands in $100 - 300$ cm^{-1} are due to S-S-S bending, while the stretching bands in $400 - 500$ cm^{-1} are ascribed to S-S bending. For the porous carbon, two broad peaks were observed at 1350 and 1580 cm^{-1} corresponding to disordered (D) and graphitic (G) carbon, respectively, testifying that the porous carbon is partially graphitized. Strong sulfur peaks were displayed for the mixed C/S composite (Figure 20), which is consistent with S$_8$. However, these sulfur peaks disappeared after 5 minute irradiation of Raman laser, showing that pristine S$_8$ suffers severe sublimation. In contrast to the mixed C/S sample, no sulfur peaks appeared for the high-temperature C/S composite. Instead, a similar shape to the pure porous carbon was observed (Figure 19). The reason is that Raman is a surface analytic technique and the trace amount of S$_8$ (revealed by the TGA measurement) on the surface of the porous carbon is sensitive to sublimation, thus only carbon signal was detected. To collect signal of sulfur inside of pore, the high-temperature C/S composite was ball-milled for 10 minutes to break the particle. Only one peak at 479 cm^{-1} was observed (Figure 19), which is due to S-S stretching mode. The absence of stretching bands of S-S-S for the high-temperature C/S composites clearly suggests that the confinement of the porous carbon remarkably changed the form of sulfur. Therefore, we

25

hypothesize that, instead of S_8, smaller molecules of S_2 were trapped in the small pores through bond between S and C in the high-temperature C/S composite.
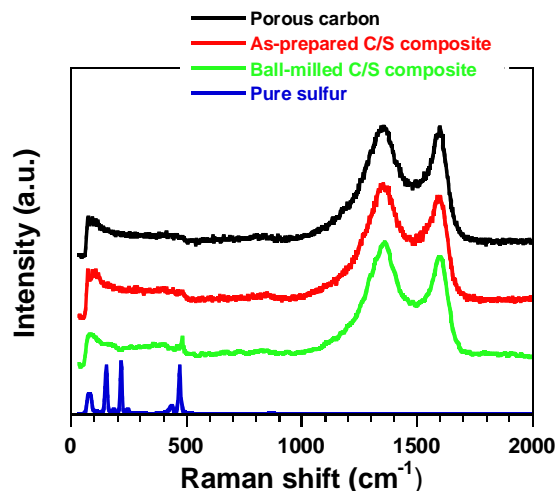

Figure 19. Raman spectra of pure sulfur, mesoporous carbon and high-temperature porous C/S composite.
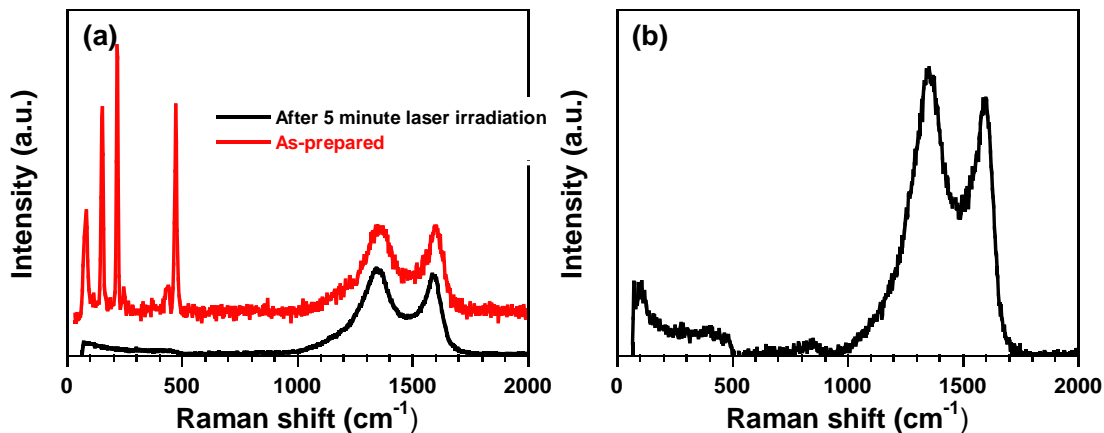

Figure 20. Raman spectra of (a) as-prepared high-temperature C/S composite and (b) porous carbon/sulfur mixture before and after 5 minute Raman laser irradiation.

The interaction of C/S was further investigated using time-of-secondary ion mass spectrometry (TOF-SIMS), which is a powerful surface sensitive technique with ppb sensitivity across the periodic table. In TOF-SIMS analysis, the C/S composite sample surface was bombarded with a pulsed primary ion beam, which generates neutrals and secondary ions. These secondary ion masses were measured by a time-of-flight mass detector. TOF-SIMS data were collected on a TOF.SIMS 5 analyzer using a liquid metal Bi_1^+ ion gun at the operation energy of 30 KeV. The collection time is 300 s at a sample current of 1.9 pA and analysis area of 500 ×

26

500 μm^2. Data were collected in both negative and positive ion polarity. Table 1 lists selected mass relative intensities of the detected ions which are normalized to the total ion intensity. The results revealed that the signal of S$^-$ is the dominant one for sulfur following by S$_2^-$ and S$_3^-$, and trace amount of larger sulfur negative ions were also observed. But there is no S$_8$ detected by the TOF-SIMS method. As for the carbon-related species, C$^-$ ions are the major fragments. It is clear that the TOF-SIMS probe beam is strong enough to break the bond between atoms and produce secondary ion species. The interesting thing is that fragments with C-S species were clearly detected, including CS$^-$, C$_2$S$^-$, C$_3$S$^-$ and CS$^+$, as shown in Table 1. This strongly demonstrates the existence of C-S bond in the C/S composite and the bond is strong enough to survive the TOF-SIMS beam bombarding. The C-S bond is believed to play a critical role in trapping sulfur in the mesoporous carbon matrix, thus providing stabilized sulfur as cathodes for good electrochemical performance in Na-S batteries.

Table 1. Relative intensities of the secondary ion species probed by the TOF-SIMS method. The intensities are normalized to the total ion intensity.

Ions	Mass	Intensity
C$^+$	12	18.10
C$^-$	12	438.00
S$^-$	32	740.00
S$_2^-$	64	62.60
S$_3^-$	96	29.60
S$_4^-$	128	3.43
S$_5^-$	160	0.27
S$_6^-$	192	0.11
S$_7^-$	224	0.02
S$_8^-$	256	-
CS$^-$	44	8.89
C$_2$S$^-$	56	29.70
C$_3$S$^-$	68	2.92
CS$^+$	44	1.08

4.5.2 Sulfur stability of the C/S composites

The thermal behavior of the C/S composite was investigated by thermogravimetric analysis (TGA). For comparison, pure sulfur was also measured. Data are shown in Figure 21a. It can be found that the pure sulfur has a complete sulfur evaporation at ~ 300 °C, which is similar to that reported in literature. Quite different from the mixed sample, the high-temperature C/S composite shows response at much higher temperature in the TGA analysis with two weight

losses, one is below 250 °C with a small amount of weight loss and the other one between 400 °C and 500 °C with main weight loss. The weight loss at the low temperature is probably due to the evaporation of cyclic S_8 on the surface of the porous carbon, while the weight loss at high temperature suggests the S_2 formed at 600 °C was confined in the carbon mesopores and bonded with carbon at room temperature.

The cyclic sulfur also suffers severe sublimation in the ultra-high vacuum (UHV) as evidenced by X-ray photoelectron spectroscopy (XPS) instrument, in which samples were loaded into the test chamber and evacuated to a pressure of ~1x 10^{-8} Torr and left overnight before collecting data. Figure 21b shows the XPS spectra of the high-temperature and mixed C/S samples. For comparison, these spectra were normalized at the carbon peaks. Strong sulfur peaks were observed for the high-temperature C/S composite, in which the sulfur content was calculated to be 20 wt%; while the mixed C/S sample with S_8 shows very weak sulfur peaks with sulfur retention of only 2 wt%. This demonstrates a superior stability of the high-temperature C/S composite with respect to sublimation under UHV conditions. Even after many hours stay in the UHV chamber there is no obvious sublimation of sulfur for the C/S composite (Figure 21b), which reveals that the sulfur is strongly confined in the porous carbon.
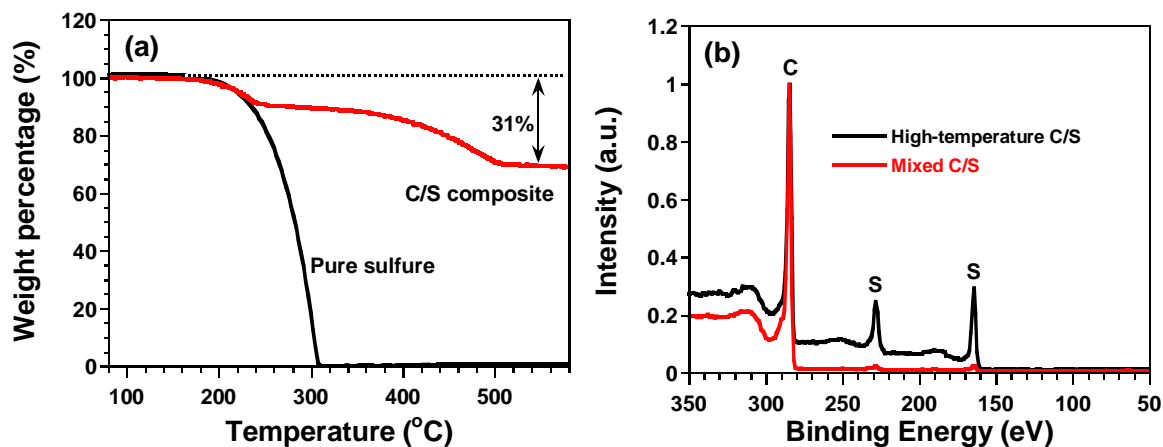

Figure 21. Sulfur stability of the C/S composites. (a) TGA curves of the high-temperature and pure sulfur, and (b) XPS spectra of high-temperature and mixed porous C/S composites.

Although quite a number of works based on carbon/sulfur composite cathodes have been presented for Li-S batteries with improved performance, there is no study on the sulfur electrodes using microcopy techniques due to the sublimation of sulfur under vacuum and probe

beam irradiation. The stability of sulfur of the high-temperature C/S composite was characterized using different microcopy techniques.

The stability of the high-temperature C/S composite was further investigated using electron beam irradiation inside TEM. The pristine sulfur or C/S composite particles were dispersed on TEM grid, loaded into TEM machine and further exposed to electron beam. The elemental composition was analyzed before and after irradiation for a time with different beam strength. The irradiation conditions and results of sulfur retention were listed in Table 2. The pristine sulfur quickly disappeared under the exposure to electron beam even with a low dose of 7.43 A/m^2 (Figure 22a). After 20 minute irradiation, only 1.92 wt% retained due to sublimation and decomposition, indicating an unstable behavior. This is consistent with XPS measurement. The low-temperature C/S composite prepared at 150°C, also suffered a drastic decrease in sulfur content. 0.84 wt% remained after 30 minute beam irradiation with a medium dose of 74.2 A/m^2 (Figure 22b). In contrast to the pristine sulfur and low-temperature C/S composite samples, the high-temperature C/S composite demonstrated a super stability. After an electron irradiation of 30 minutes at a moderate dose of 74.6 A/m^2, which is similar to that used for the C/S composite prepared at 150 °C and about 10 times larger than that used in pure sulfur, or 20 minutes at a strong dose of 796 A/m^2, sulfur retentions are 32.28 wt% and 31.34 wt% (Figure 22d and e), respectively. If taking into account the system error, no sulfur loss occurred in comparison with the as-prepared sample (Figure 22c). Surprisingly, even under extremely strong electron beam exposure (with a dose of 35000 A/m^2) for 20 minutes, 22.93 wt % sulfur still remains (Figure 22f). The results clearly suggest that for the high-temperature C/S composite, sulfur was strongly confined and bonded in the carbon pores, which provides strong resistance to the electron beam irradiation and prevents sulfur from sublimation in the high vacuum and decomposition under 300 keV electron irradiation.

Table 2. Electron beam irradiation in TEM. S content retention after irradiation of electron beam at different electron doses and different irradiation time.

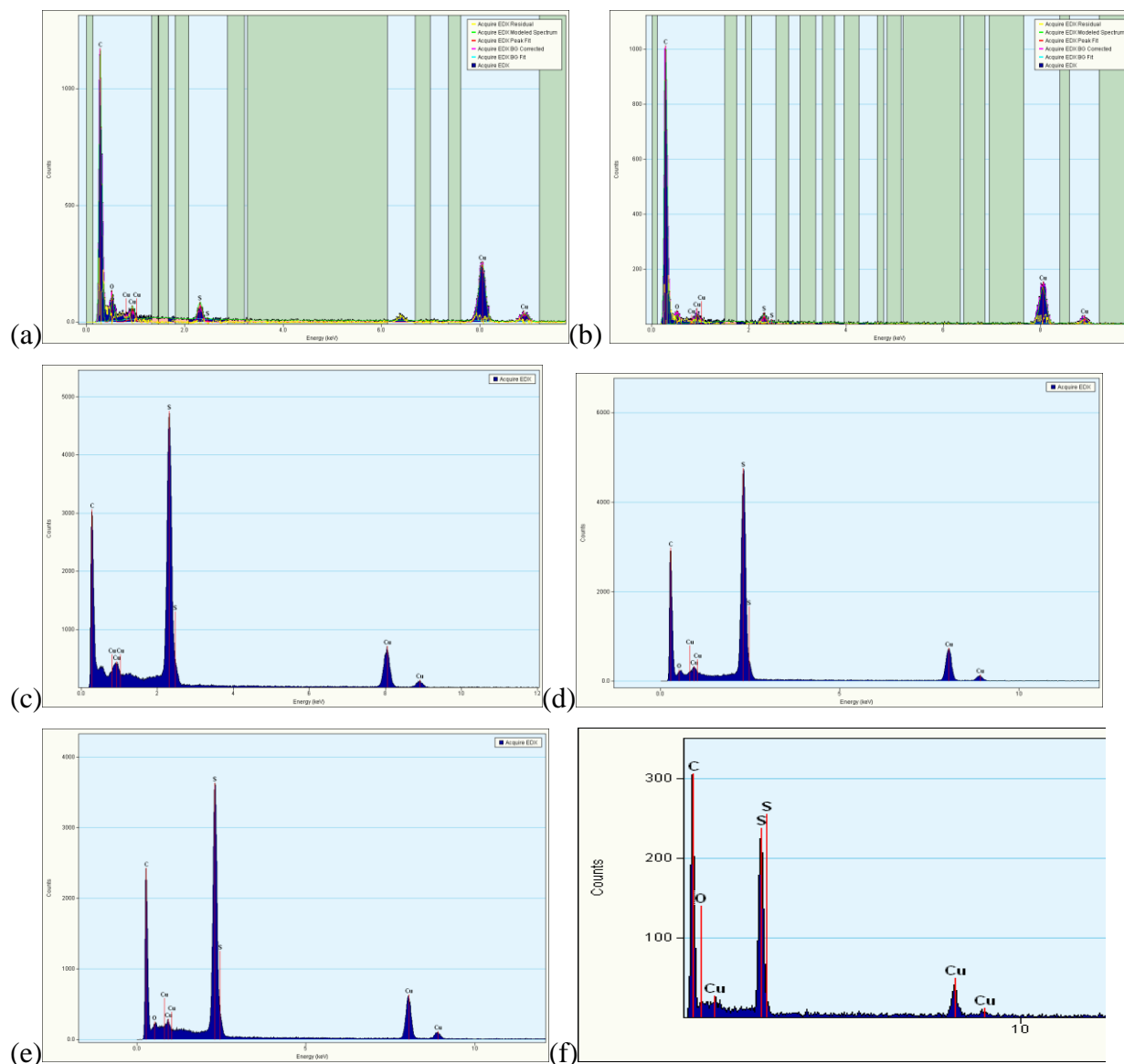| Samples	Electron dose (A/m^2)	Irradiation time (min)	Sulfur retention (wt%)
Pure S	7.43	20	1.92
Low-temperature C/S composite	74.2	30	0.84
High-temperature C/S composite	74.6	0	31.73
High-temperature C/S composite	74.6	30	32.28
High-temperature C/S composite	796	20	31.34
High-temperature C/S composite	35000	20	24.28

Figure 22. EDX spectra with the elemental analysis of (a) pure sulfur after 20 min radiation of electron beam with a low dose of 7.43 A/m^2, (b) low-temperature mesoporous C/S composite after 30 min radiation of electron beam with a low dose of 74.2 A/m^2, (c) as prepared high-temperature mesoporous C/S composite, (d) the high-temperature mesoporous C/S composite after 30 min radiation of electron beam with a moderate dose of 74.6 A/m^2, (e) the high-temperature mesoporous C/S composite after 20 min radiation of electron beam with a strong dose of 795 A/m^2, and (f) high-temperature mesoporous C/S composite after 20 min radiation of electron beam with an extremely strong dose of 35000 A/m^2.

4.5.3 Electrochemical performance

Electrochemical performance of the mesoporous C/S composite was investigated as cathode for Na-ion batteries in coin cells, shown in Figure 23. The C/S composite was mixed with carbon black and sodium carboxymethyl cellulose (CMC) binder to form slurry, and then cast on the current collector of an aluminum foil. Sodium metal was used as the counter electrode. Cells were assembled with electrolyte of $NaClO_4$ dissolved in a mixture of ethylene carbonate/diethyl carbonate (EC/DEC, 1:1 by volume). Figure 23a shows the voltage profiles in the first two cycles at a scan rate of 80 mA/g between 0.8 V and 2.5 V. A small plateau at 2.15 V (insert in Figure 23a) and a lower one at 1 V were displayed in the first cycle. Typically, Na-S batteries show two discharge plateaus at 2.28 V and 1.73 V, respectively. The former one corresponds to the reaction of $S_8+Na\rightarrow Na_2S_n$ ($n\geq4$); while the later is related to the formation of Na_2S_n ($n<4$). The small plateau at 2.15 V is associated with the formation of Na_2S_n ($n\geq4$), indicating that a trace amount of cyclic S_8 exists on the surface of porous carbon, which is consistent with the TGA results. However, the high voltage plateau at 2.15 V disappeared and the low-voltage plateau at 1.0 V change to a slope line centered at 1.2 V in the second cycle. This means that a different reaction mechanism from the conventional Na-S batteries, which is similar to charge/discharge behavior in Li-S batteries, but at a low voltage. The first discharge delivered a capacity of 1407 mAh/g, approaching the theoretical value of 1675 mAh/g assuming fully desodiated Na_2S formed. The reversible capacity is 860 mAh/g. Taking into account the high conductivity of the mesoporous carbon matrix, these results demonstrate high utilization of sulfur in this work.
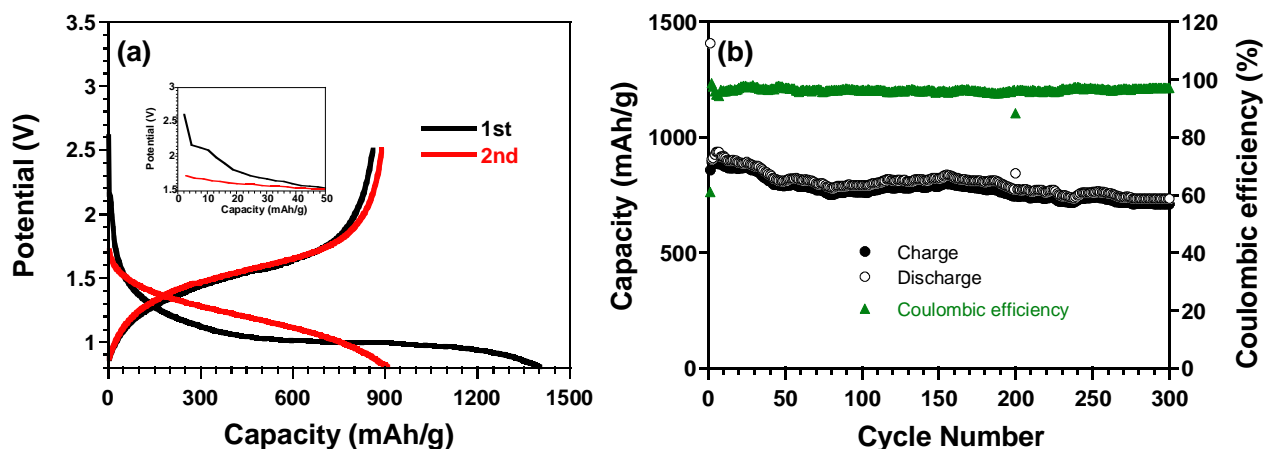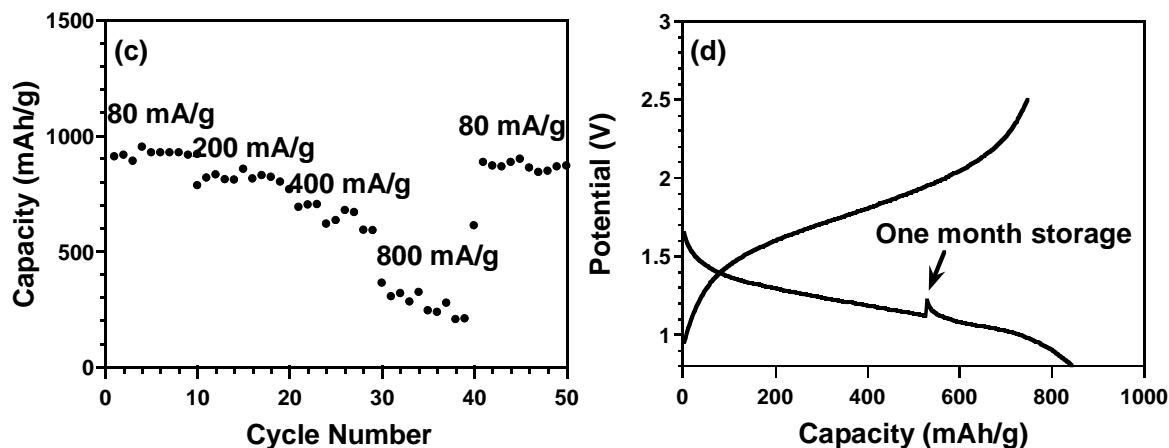
Figure 23. Electrochemical performance of the C/S composites in Na-S batteries. (a) Voltage profiles, (b) cycling performance and Coulombic efficiency, (c) rate performance of the mesoporous C/S composite cathodes for Na-S batteries, and (d) self-discharge behavior of S/C cathode in a month storage in cell. Insert: enlarged charge/discharge curves from the marked area in panel (a).

The long cycling stability was evaluated by charging/discharging the Na-S cells at room temperature with a current of 80 mA/g between 0.8 – 2.5 V. Results are shown in Figure 23b. An exceptional stability was demonstrated for the porous C/S composite. The desodiation capacity retention is as high as 712 mAh/g after 300 cycles, which corresponds to 83% of that in the first cycle (860 mAh/g) and results in a pretty low capacity loss of 0.05% each cycle. In particular, unlike the conventional sulfur cathodes in Li-S batteries, where low efficiency and poor cycle life originated from the severe dissolution of polysulfides and shuttling behavior, the porous C/S composite delivered a high Coulombic efficiency of ~97% over 300 cycles except the first cycle (Figure 23c). This reveals that the S_2 imbedded into the porous carbon was effectively "stabilized" in the small voids, thus the dissolution and shuttling effects of high order polysulfides were completely prevented. The rate capability was also checked at higher current density, shown in Figure 23d. A capacity of about 250 mAh/g was retained at 800 mA/g. The C/S composite cathodes for Na-S batteries in literature can only provide 500 mAh/g, and the capacity quickly decreases to 200 mAh/g within 10 charge/discharge cycles. To the best of our knowledge, such long cycling lifetime, high capacity, high efficiency and good rate capability, so far, has not been reported. It clearly demonstrates that the high-temperature porous C/S composites are promising cathode materials for Na-S batteries.

4.5.4 Discussion

Since only high order polysulfides (NaS_n, $n \geq 4$) are soluble in liquid electrolytes and lower Columbic efficiency and cycling stability, if the sulfur exists as S_2 and stabilized in a host material, insoluble low order polysulfides (NaS_2 and Na_2S) will form during sodiation, thus improving the cycling stability and Columbic efficiency. However, it is a challenge to synthesize C/S_2 composite. At room temperature, sulfur exists mainly in the form of cyclooctasulfur (S_8). But at elevated temperature, the cyclic molecules can be broken into smaller species, including chain molecules from S_2 to S_8. Upon increase in temperature, the concentration of S_8 steadily decreases along with increase in small sulfur allotropes. Particularly, in sulfur vapor above 600 °C at low pressure of 1 torr, S_2 is the most abundant species, accounting for 99% of all vapor species (S2, S4, S6, and S8). If there is no further treatment, S_2 molecules will recombine to form cyclo-S_8 when cooling down to room temperature. It has been found that small sulfur species can be trapped individually in pores with suitable pore size in a host matrix. This offers us a great opportunity to facilely produce small sulfur species at high temperature and vacuum conditions. In this study, mesoporous carbon was used as the host material to trap small sulfur molecules produced at 600 °C under vacuum. The electrochemical measurement results show that the C/S composite preserved the form of small sulfur molecules. A small amount of S_2 on the surface of porous carbon particles changed back to S_8, as revealed by the short voltage plateau at 2.15 V in the first sodiation (insert in Figure 23a) and the TGA measurement results. The disappearance of short voltage plateau at 2.15 V from the second sodiation suggests that the high order polysulfides formed by sodiation of S_8 dissolved into electrolyte. It should be noted that the Raman spectra of the carbon/sulfur composite didn't show signals of S-S-S stretching bands. Instead, only one stretching band at 479 cm^{-1} appeared which is due to S-S stretching mode. These results suggest that there is strong interaction between carbon and sulfur. The C-S bond was also confirmed by the TGA response at higher temperature (Figure 21a). Actually, previous studies have found that, relative to the cyclo-S_8, smaller sulfur molecules with chain structures showed much higher chemical reactivity due to the free-radicals at the ends of sulfur chains.[11] The free-radicals make short chain sulfur species extremely active toward almost every chemical, including carbon. Therefore, small sulfur species, mainly S_2, produced at 600 °C were confined in the small carbon voids as a result of the strong interaction between carbon and sulfur, which is

consistent with the Raman, XPS, TGA, TEM and TOF-SIMS measurement results (Figure 19, 20, and 21, Table 1 and 2). The C-S bond enables the confined sulfur to resist the probe beam irradiation, thermal and vacuum process, consequently provides stable sulfur cathodes for electrochemical cycling even with liquid electrolytes.

The elimination of cyclo-S_8 and strong C-S binding in the mesoporous C/S composite were also evidenced by the absence of 2.28 V discharge plateau, which corresponds to the formation of sodium polymersulfides Na_2S_n (n≥4), and the slope shaped charge/discharge profiles in the second charge/discharge cycles (Figure 23a). Therefore, the production of soluble intermediate polymersulfides, which is responsible for the poor cycling performance and low capacity observed in Na-S and Li-S batteries with liquid electrolytes, is practically prevented. It is noted that 1.73 V plateau related to the formation of NaS_2 and Na_2S is also absent for the C/S composite. Instead, a discharge slope at a lower potential appeared, which shows that the C/S composite has different reaction mechanism from the cyclic S_8. This could be attributed to C/S the binding effects. The chemical interaction would lead to a high electrochemical polarization and thus require additional energy to form sodium sulfides, which drives the sodiation reaction to a lower discharge voltage than cyclo-S_8. After the first cycle, less strain leads to a higher discharge voltage and the C-S bond makes the sodiation behavior of S_2 in the second cycle similar to Na insertion into solid solution phase, i.e. a slop voltage line. Similar results have been reported for other C/S composites and metal sulfides, such as Ni_3S_2 and FeS_2, in which S was bonded with metals. The confined small sulfur molecules (mainly S_2) and strong binding of C/S effectively exclude the dissolution behavior of sodium polysulfide intermediates. As a result, superior stability of sulfur cathode to room temperature Na-S batteries using liquid electrolytes was demonstrated (Figure 23).

4.6 Solid electrolyte interface film protected sulfur cathodes with superior cycle stability for lithium-ion batteries

4.6.1 Synthesis and characterization of sulfur cathodes.

S_2 was impregnated into the mesoporous carbon using a vapour-infusion method developed by our group. Sulfur was mixed with porous carbon at different ratios of C/S, 80/20, 60/40, 40/60, and 20/80 by weight, denoted as S20, S40, S60, and S80, respectively. The mixtures were sealed in glass tubes under vacuum and underwent heat treatment at 600 °C to produce S_2. At

this temperature, S_2 is the dominate sulfur species in the sulfur vapour. The resulting S_2 can be impregnated into the porous carbon and maintained S_2 form when cooling down. By comparing the weight before and after heat treatment, the component ratios of the final products were determined to be 15%, 31%, 55%, and 75% for S20, S40, S60, and S80, respectively.

The elemental mapping images of the C/S composites in Figure 24 show that sulfur is homogenously distributed in the porous carbon spheres, demonstrating a perfect S_2 infiltration into the mesoporous carbon. The uniform distribution and good conductivity of the porous carbon ensure a good kinetics for the C/S_2 composite cathode. The selected area electron diffraction (SAED) was performed on the four different component C/S composites, shown in Figure 1d, h, l and p. Only broad diffraction rings were displayed for all of them, indicating that there is no crystalline sulfur in the porous carbon matrix. It was noted that no sulfur accumulation on the surface was detected even for the high sulfur content samples. The reason is possibly that sulfur on surface suffers sublimation under vacuum and probe beam irradiation.
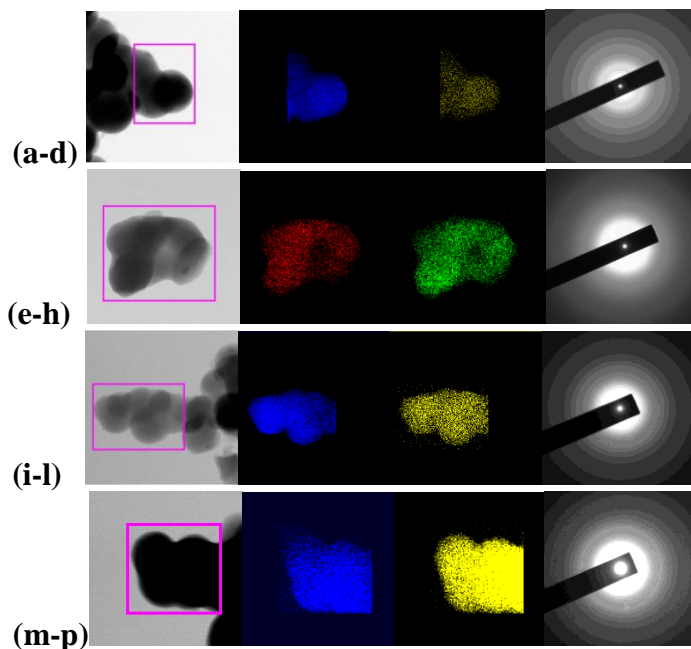

Figure 24. TEM, elemental mapping, and SAED images of (a-d) S20, (e-h) S40, (i-l) S60 and (m-p) S80.

X-ray diffraction (XRD) pattern was analyzed for the C/S composites, pure suflur and porous carbon. Data are shown in Figure 25a. The pristine suflur shows well-defined diffraction peaks that correspond to the crystalline structure of cyclic S_8. The C/S composites with low sulfur content, such as S20 and S40, display similar diffraction pattern to the pure mesoporous carbon. The absence of S_8 peaks in XRD pattern revealed a different sulfur existence form for the C/S_2

composites. In contrast, the high sulfur-content samples (S60 and S80) clearly show the same well-defined diffraction peaks as those pristine S_8, revealing that accumulated crystalline S_8 exists on surface, which confirms our guess from the observations in TEM SAED results.

The difference between pristine S_8, porous carbon, and the C/S composites was also observed in the Raman spectra shown in Figure 25b. For the porous carbon, two peaks were observed at 1350 and 1580 cm^{-1} corresponding to disorder (D) and graphitic (G) carbon, respectively, which indicates that the porous carbon is partially graphitized. For the pristine S_8, typical Raman spectrum pattern was presented in Figure 25b. However, the low sulfur-content C/S composites of S20 and S40 don't show any sulfur peak except the peaks of the pure porous carbon although elemental mapping (Figure 24) confirmed the existence of sulfur in the porous carbon. The absence of characteristic peaks of S_8 in the Raman spectra suggests that the existence of strong interaction between carbon and sulfur failed the signal probe of Raman activity (Figure 25a). The strong sulfur peaks of S60 and S80 identify the existence of cyclic S_8. The XRD and Raman results suggest that sulfur embedded within the porous carbon spheres exists in a different form from cyclic S_8; while sulfur accumulated on the surface has the general cyclic structure of S_8. In addition, S40 has a saturated sulfur filling inside the porous carbon without sulfur accumulation on surface, and the best electrochemical performance is anticipated.

At room temperature, cyclooctasulfur (S_8) is the main and stable form of sulfur. But at elevated temperature, the cyclic molecules can be broken into smaller species and the concentration of smaller sulfur species increases with temperature. For example, S_2 accounts for 99% of all sulfur vapour species (S_2, S_4, S_6, and S_8) at temperatures above 600 °C. Since cyclo-S_8 is a thermodynamically stable structure at room temperature, the high-temperature-produced S_2 molecules will recombine to form cyclo-S_8 when temperature is cooling down. It has been proposed that small sulfur species S_2 can be preserved in a host matrix at room temperature. In this work, the mesoporous carbon functions as the host material to trap S_2 produced at 600 °C and stabilize the metastable S_2 at room temperature. The absence of S_8 signal in Raman and XRD data clearly revealed that the mesoporous carbon can effectively suppress the reformation of S_8 from S_2. Therefore, we conclude that S20 and S40 consist of only S_2 molecules, but S60 and S80 contain both S_2 and cyclic S_8.

The porous C/S composites, pure porous carbon and pristine S_8 were further characterized by

X-ray photoelectron spectroscopy (XPS) as shown in Figure 25c. In the XPS measurement, samples were loaded into the test chamber and evacuated to a pressure of ~1x 10^{-8} Torr. The pristine cyclic S_8 suffered severe sublimation under the ultra-high vacuum during the XPS measurement, which is evidenced by the absence of sulfur signal of pure S_8 in Figure 25c. In contrast, strong sulfur peaks were observed for the porous C/S composites, demonstrating that S_2 is stable in the porous carbon under the ultra-high vacuum. The high stability of S_2 in the porous carbon suggests that the S_2 molecules were strongly confined within the porous carbon.

XPS is a precise and surface sensitive chemical analysis technique. During XPS measurement, the electrons will loss energy as they pass a thin solid layer in the surface region, which contributes to the background. Therefore, the distribution information of sulfur in the surface area of the porous carbon can be obtained by comparing the ratio of photoelectric peak area to the increase in background in the S 2p region. The ratios were calculated using the equation

$$D=I_{S\ 2p}/B$$

where $I_{S\ 2p}$ is the S 2p peak area and B is the increase in background measured at 50 eV to higher binding energy of the S 2p peak. The linear background was taken from a binding energy of 50 eV lower and 20 eV higher than the S 2p peak. The ratios for the C/S composites with different suflur loading are depicted in Figure 25b. It can be seen that S40 has the smallest ratio (1.36), while S20, S60 and S80 are 1.73, 1.71 and 1.83, respectively. The lower ratio value indicates a greater amount of electrons escape from the deeper region within the surface. It is worth noting that although S60 and S80 have much higher suflur content than S20, they show similar ratio values, meaning that they have similar sulfur distribution in the surface. The sulfur distribution for the C/S composites with different sulfur contents is schematically illustrated in Figure 25e-h. For low suflur loading sample of S20, a thin layer of sulfur is uniformly coated on the surface of the porous carbon and walls of the carbon pores (Figure 25e). As sulfur increases, the carbon pores are filled with sulfur, as shown in Figure 25f for S40, in which all pores are fully filled and there is no extra sulfur accumulated on the surface. S80 has a thicker layer of sulfur on the surface. On the basis of the measurement mechanism of XPS, S20, S60 and S80 have the similar flat surface morphology of sulfur, i.e. uniform layer distribution. Therefore, similar ratio values were observed for S20, S60 and S80. The XPS results and the illustration in Figure 25e suggest

37

that sulfur is well trapped in the pores for S40, which is the preferred architecture for sulfur cathodes and expected to provide good performance.
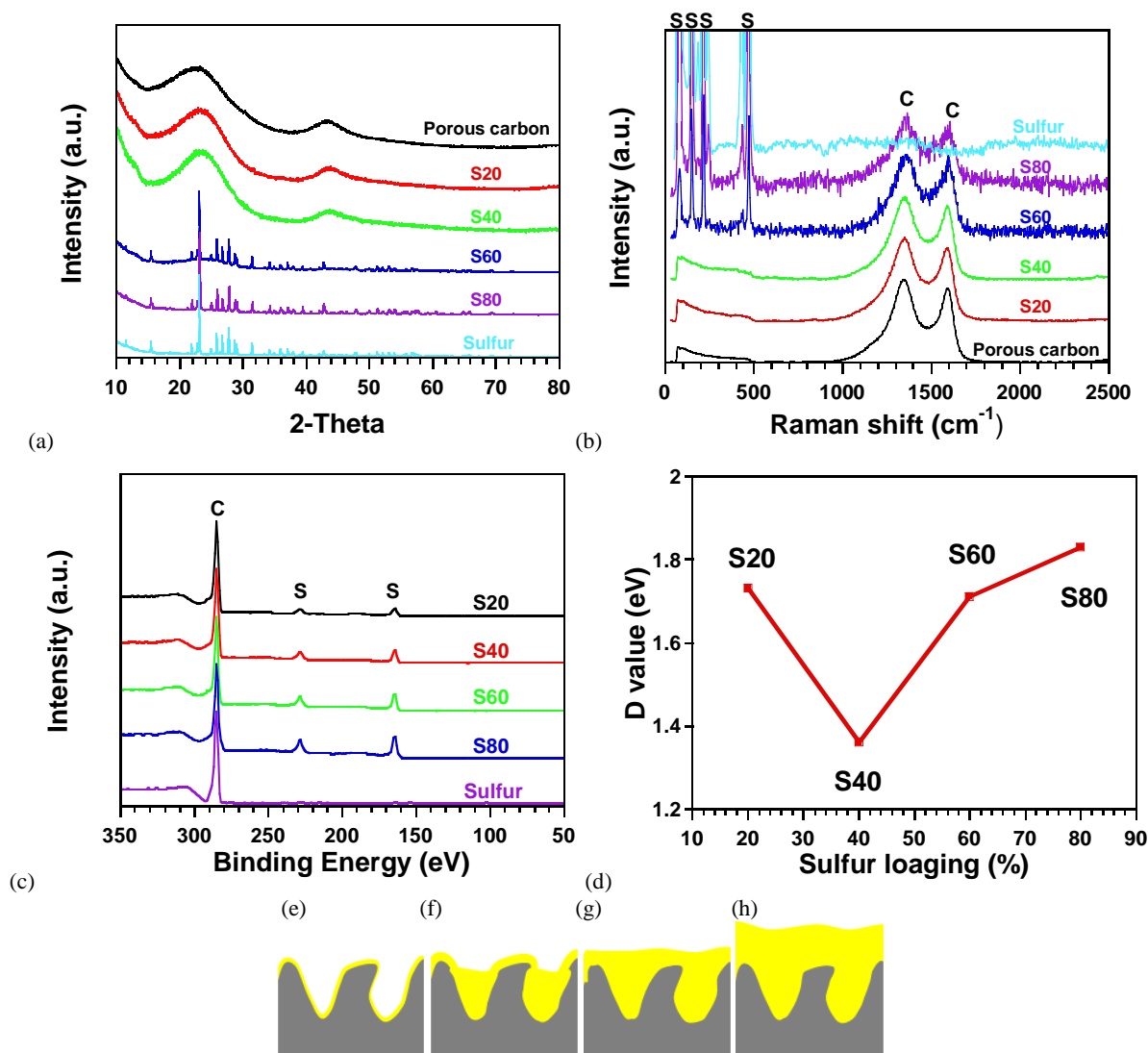

Figure 25. (a) XRD, (b) Raman, (c) XPS, and (d) curves of D value variation vs sulfur loading by XPS, and (e-h) schematic illustration of sulfur filling level at different sulfur content.

4.6.1 Electrochemical performance

The electrochemical performance of the C/S composite cathodes with different C/S ratios was investigated in coin cells using lithium metal as a counter and reference electrode. Two kinds of electrolytes, carbonate-based of 1M $LiPF_6$ in a mixture of ethylene carbonate/diethyl carbonate (EC/DEC, 1:1 by volume), and ether-based of 1M lithium bis(trifluoromethylsulfonyl)imide (LiTFSI) in tetra(ethylene glycol) dimethyl ether (TEGDME),

were used to study the influence of electrolytes on the electrochemical performance. The C/S composite cathodes were prepared by mixing C/S powders with carbon black and sodium carboxymethyl cellulose (CMC) binder to form slurry, and then cast on an aluminum current collector. Figure 26a and b show the charge/discharge profiles of C/S cathodes in the first cycle with carbonate- and ether-based electrolytes, respectively. The profiles of the second cycle are shown in Figure 27. For the low sulfur loading cathode of S20, similar voltage profiles were displayed for both electrolytes with a long plateau at 1.20 V in the first discharge and very low capacity afterward. Similar behaviour was observed for S40. A long discharge plateau appeared at 1.50 V in the first cycle for both carbonate- and ether-based electrolytes, and then it presents a charge slope around 2.0 V and a discharge slope at 1.60 V. However, the electrolytes have significant influence on the electrochemical performance for the high sulfur loading composites (S60 and S80). For example, with carbonate electrolyte they present two plateaus at 2.44 V and 1.60 V in the first discharge and then nothing left for S80 and low capacity for S60 with slope voltage profiles in the following cycles (Figure 26a and 27a). While the ether electrolyte show completely different behavior. Two plateaus at 2.44 V and 2.05 V, respectively, and a slope at 1.6 V were obtained in all discharge processes. The former two plateaus are characteristic of cyclic S_8 due to the formation of high and low order polysulfides, respectively, which is attributed to the surface-accumulated sulfur. The lower slope is same as those observed for the low sulfur loading composites and is associated with the carbon-confined sulfur inside the porous carbon spheres. The absence of the plateau at 2.4 V for S40 confirms that cyclic S_8 does not exist, which is consistent with the Raman and XRD measurement results. The elimination of cyclic S_8 avoids the formation of soluble intermediate polysulfides. The lower reaction potention has been reported for Li-S batteries by several groups and was ascribed to the lithiation reaction to form insoluble sulfides, Li_2S_2 and Li_2S. In our case, the lithiation process is a solid state reaction with the following equations:

$$S_2 + 2Li^+ \rightarrow Li_2S_2$$

$$Li_2S_2 + 2Li^+ \rightarrow 2Li_2S$$
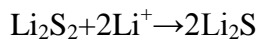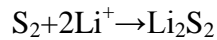
It is believed that the strong interaction between S_2 and carbon drive the lithiation reaction to a lower discharge potential, and also makes the lithiation profile a slope shape.
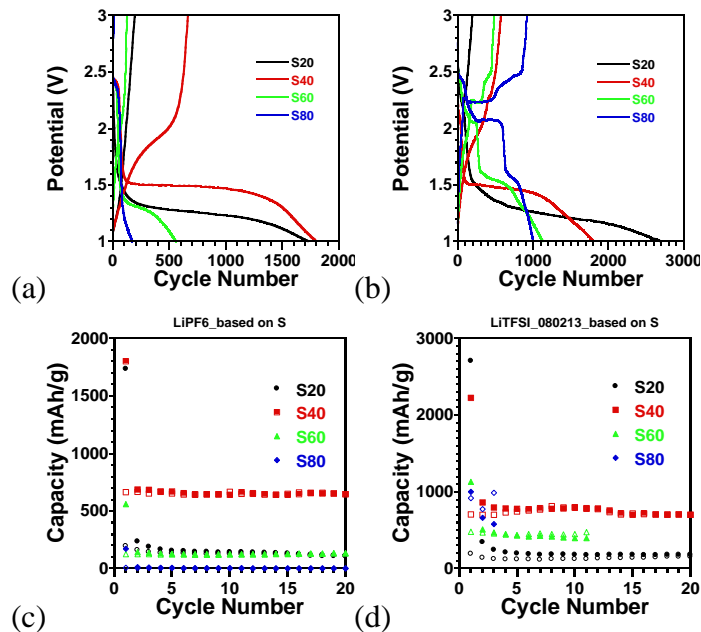
Figure 26. Voltage profiles of the C/S cathodes in the first cycle with (a) carbonate- and (b) ether-based electrolytes and cycling performance of the C/S cathodes with (c) carbonate- and (d) ether-based electrolyte.
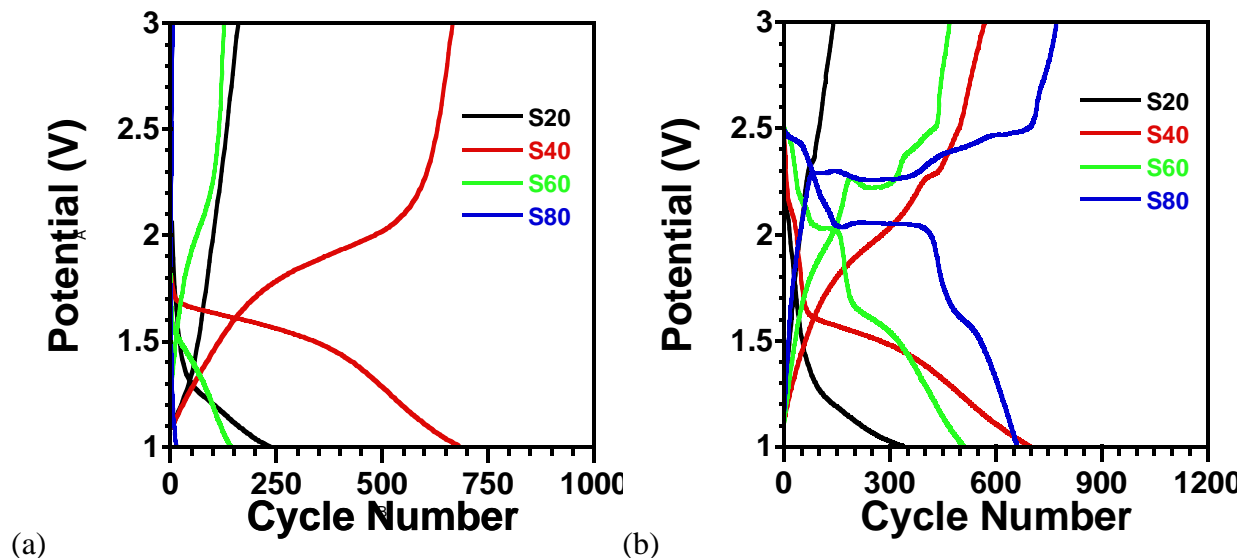

Figure 27. Voltage profiles of the C/S cathodes in the second cycle with (a) carbonate- and (b) ether-based electrolytes.

Table 3 lists the charge/discharge capacities and Coulombic efficiencies of the C/S composites in the first cycle with two kinds of electrolytes. Low Coulombic efficiencies were observed with carbonate electrolyte in the first cycle for all C/S cathodes, 14.4%, 36.9%, 23.3% and 7.0% for S20, S40, S60 and S80, respectively. Different mechanisms are responsible for the low and high

sulfur loading composites. For the low sulfur content samples, the large irreversible capacities of 1539.0 mAh/g and 1136.5 mAh/g for S20 and S40, respectively, are mainly attributed to the formation of SEI films as a result of the decomposition of electrolyte; while for the high sulfur content samples, it's due to low solubility of high order polysulfides in the carbonate electrolyte and the electronically and ionically insulating nature of elemental sulfur and insoluble low order polysulfides (Li_2S and Li_2S_2), which isolate the sulfur particles, thereby losing electrochemical activity. The ether electrolyte shows similar performance to carbonate electrolyte for S20 and S40, low Coulombic efficiencies of 10.1% and 31.7%, large capacity loss of 2512.3 mAh/g and 1519.9 mAh/g, respectively. However S60 and S80 have much higher efficiencies than carbonate electrolyte, 42.6% and 92.5%, respectively, indicating higher sulfur utilization for ether electrolyte than carbonate electrolyte.

Table 3. Charge/discharge capacity and Coulombic efficiency of the C/S composites with different electrolytes in the first cycle.

	Carbonate electrolyte			Ether electrolyte		
	Discharge capacity (mAh/g)	Charge capacity (mAh/g)	Coulombic efficiency (%)	Discharge capacity (mAh/g)	Charge capacity (mAh/g)	Coulombic efficiency (%)
S20	1733.2	194.2	14.4	2704.4	192.2	10.1
S40	1801.4	664.9	36.9	2223.9	704.1	31.7
S60	558.3	125.3	23.3	1129.6	481.7	42.6
S80	172.0	7.7	7.0	1001.4	916.0	91.5

The cycling performance of the C/S cathodes was examined with both carbonate and ether electrolytes. Stability is shown in Figure 26c and d, respectively, and Coulombic efficiency is shown in Figure 28a and b. With carbonate electrolyte, S40 shows the highest capacity of about 650 mAh/g with a Coulombic efficiency of ~100% from the second cycle, demonstrating good stability and high reversibility. The low capacity of S20 indicates that most sulfur was consumed to form SEI films, while S80 failed to deliver capacity due to the isolation of sulfur and insoluble sulfides. With ether electrolyte, S80 shows the highest reversible capacity but quickly failed due to severe shuttle reaction. After 3 cycles, it cannot be charged. S60 has better stability but also suffers obvious shuttle effects as evidenced by the quick increasing charge capacity and Coulombic efficiency in Figure 26d and 28b. Same as carbonate electrolyte, S40 is the best one for ether electrolyte with high Coulombic efficiency and a stable capacity of ~750 mAh/g, which is a little higher than its counterpart with carbonate electrolyte. This is possibly associated with

41

the higher solubility of polysufides and higher viscosity of ether electrolyte than that of carbonate electrolyte.
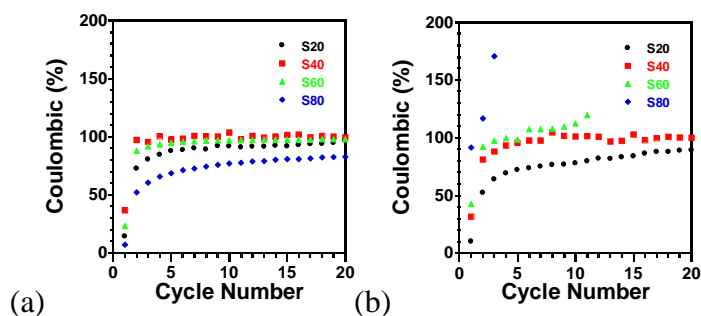

Figure 28. Coulombic efficiency of the sulfur compsotes with (a) carbonate- and (b) ether-based electrolytes.

Although ether electrolyte enhances sulfur utilization as observed in our work and proposed in literature, the severe shuttle effects due to good solubility of polysulfides preclude its use in practical Li-S cells; but carbonate electrolytes has low solubility and chemically reacts with polysulfides to form stable SEI films, thereby being thought not suitable for Li-S batteries. The SEI films were investigated by XPS measurement on cycled cathodes of S40 with both carbonate- and ether-based electrolytes. Figure 29 shows the XPS spectra for the cycled S40 cathodes with carbonate- and ether-based electrolytes. For carbonate electrolyte, the C 1s spectrum shows peaks of $C-F_2$ (291.8 eV), carbonate (290.5 eV), C-O (286.5 eV), and C-C (284.8 eV) groups. The former three peaks are from species in SEI films for LiPF6:EC:DC electrolyte. The peak at 284.8 eV is assigned to the graphitic carbon (porous carbon). A peak at 288.1 eV is a new one and not reported previously for the carbonate electrolytes. It's ascribed to

-S-C-S- (with O double-bonded to C) group, which is possibly a product of sulfur-involed decomposition reaction. The S 2p spectrum revealed that the cycled electrode contains two kinds of sulfides (Li2S2 and Li2S),

sulfone, and -S-C-S- (with O double-bonded to C) group. Sulfides were products of the reaction between S2 and lithium ions. No soluble polysulfide was detected, which confirms our speculation that only S2 exist in S40.

Sulone should be another component of SEI film. -S-C-S- (with O double-bonded to C) group is consistent with C 1s spectrum. The XPS measurement was also performed on the cycled electrodes after 10 minute

42

sputtering, shown in Figure 30. Only strong sulphide peaks remained, and all other component signals almost disappeared, clearly revealing that the cathodes were coated with SEI films on surface and there is no electrolyte penetrated into the porous carbon spheres. For ether-based electrolyte, peaks due to new species except the components of electrode, electrolyte and sulfides, showing the formation of SEI films.
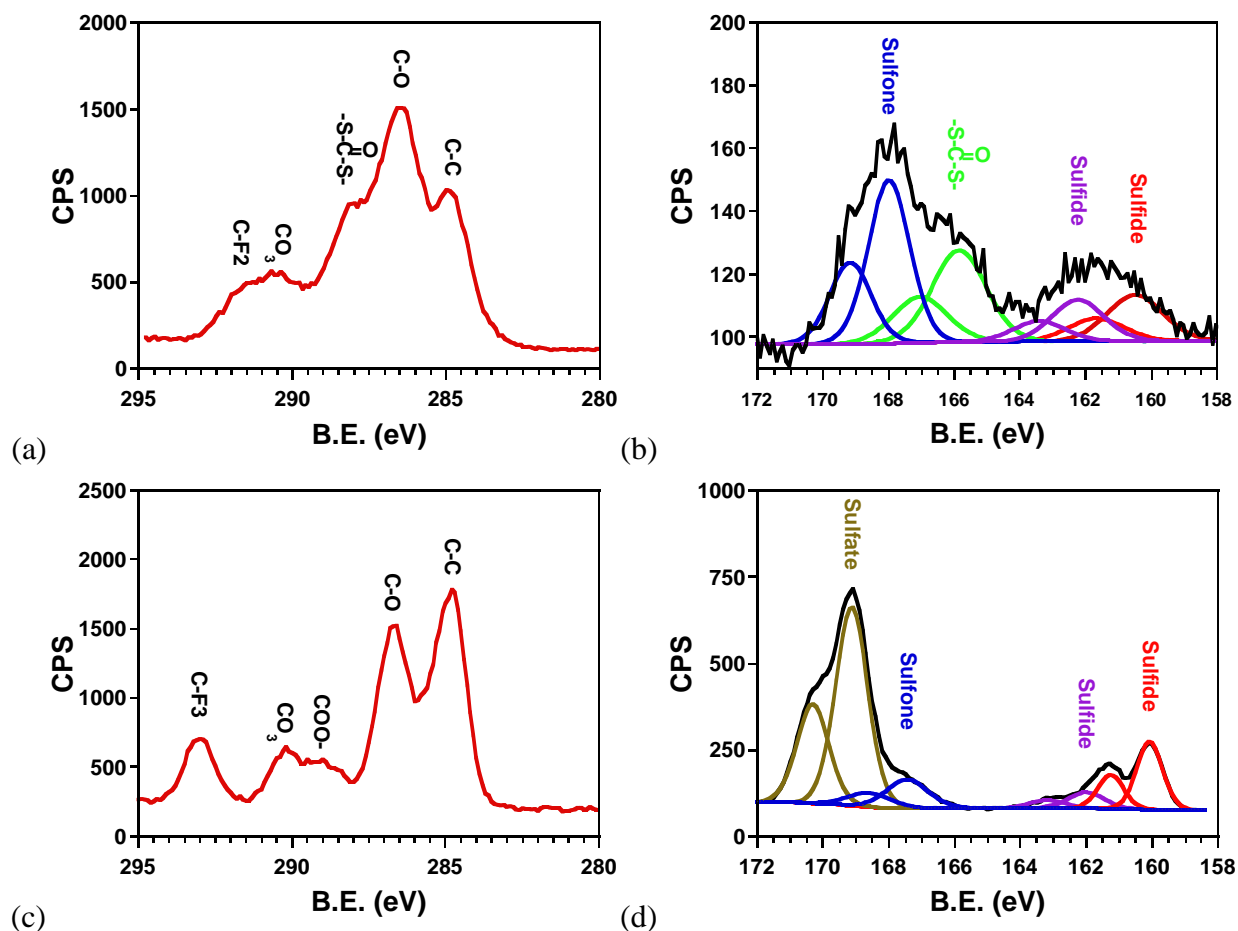

Figure 29. XPS spectra of (a,c) C 1s and (b,d) S 2p of cycled S40 cathodes cycled in (a,b) LiPF6:EC:DEC and (c,d) LiTFSI:TEGDME.

Therefore, we speculate that SEI films protect the interior sulfur from reacting with electrolytes, thus improving electrochemical performance. The long term cycling performance of S40 (Figure 30) shows that ether electrolyte has a slow capacity decrease upon advance of cycles, but carbonate electrolyte doesn't show any capacity fading. This suggests that the SEI films are not stable for ether electrolyte and the electrolyte can still penetrate through the SEI films to access the interior and reduce active sulfur. More stable SEI films were produced by the

carbonate electrolyte and completely blocked it out of the C/S spheres. The good stability of S40 is contributed not only from the confinement of porous carbon but also protection of SEI films formed on surface during electrochemical processes.
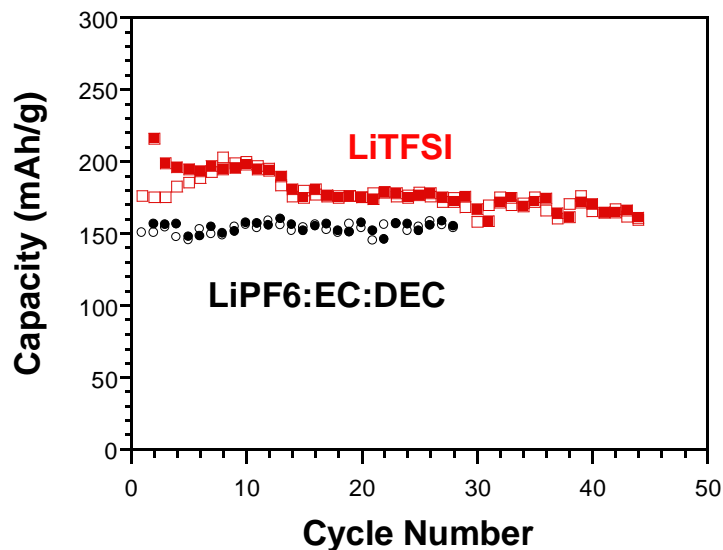

Figure 30. Cycling stability of S40 with different electrolytes.

The cycling stability of S40 was further examined by charging/discharging the cells between 1 V and 3 V at a current density of 80 mA/g for 120 cycles and then at 400 mA/g until the 2020th cycles to accelerate the cycling measurement. After 2020 cycles, the current was changed back to 80 mAh/g to check the capacity stability. There is no capacity loss observed for the C/S_2 composite during 2050 cycles, which is a new record for sulfur cathodes. In addition, Coulombic efficiency of the C/S_2 composite is close to 100% during 2050 cycles except the first cycle (Figure 31a), which is not possible for S_8 cathodes with ether electrolytes.
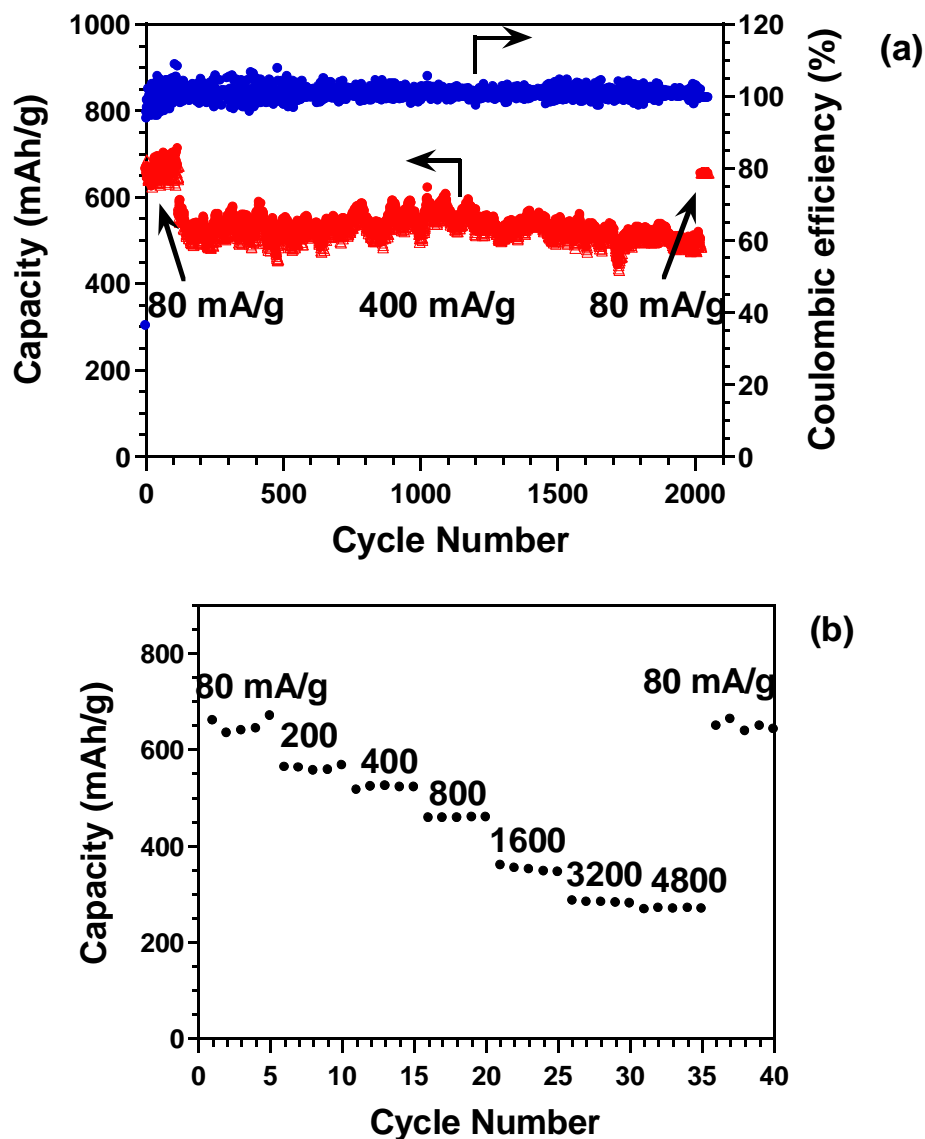
44

Figure 31. (a) cycling performance and Coulombic efficiency and (b) rate performance of the mesoporous C/S composite cathodes in Li-S batteries.

The rate capability of S40 was investigated at higher current density, shown in Figure 31b. A high capacity of about 360 mAh/g was retained at a very high current of 4800 mA/g, indicating high rate capability of the C/S composite. Such superior electrochemical performance, long cycling lifetime, high capacity, high efficiency and good rate capability, clearly demonstrate that the porous C/S composites are promising cathode materials for Li-S batteries. More importantly, carbonate electrolytes are cheaper, providing another merit, which is a particular concern for the applications in large-scale energy storage.

4.7   Nano-Structured Carbon-Coated CuO Hollow Spheres as Stable and High Rate Anodes for Lithium-Ion Batteries

4.7.1 Synthesis and characterization

The synthesis of carbon-coated hollow CuO spheres is similar to the synthesis of hollow CuO spheres as described in our previous publication.[1] The difference is the precursor solution with higher concentration of copper nitrate and sucrose was used to enable the partial carbonization of sucrose and thus to form a carbon layer on CuO particles. In details, 2.89 g of copper nitrate trihydrate ($Cu(NO_3)_2.3H_2O$, Strem Chemical), 0.51 g of sucrose ($C_{12}H_{22}O_{11}$, Sigma-Aldrich) and 15 mL of hydrogen peroxide solution (30 wt %. H_2O_2, Sigma-Aldrich) were dissolved into 45 mL of distilled water. The prepared precursor solution was atomized by a homemade collision-type atomizer using compressed air at a pressure of 0.24 MPa. The atomized aerosol droplets were passed through a silica-gel diffusion dryer first to remove the most of the solvent and then a tube furnace set at 600^oC. The normal residence time was estimated to be around 1s for a total gas flow rate of 3.5 L/min. The produced product was collected on a HTTP Millipore filter (pore size: 0.4 μm).

The morphology and architecture of the resulting products were investigated by scanning electron microscopy (SEM) and transmission electron microscopy (TEM). Images are shown in Figure 32. As shown in the SEM image in Figure 32a, the resulting products preserved the spherical morphology of the atomized precursor droplets, while the image of the broken particles (Figure 32b) revealed their hollow structure. It is also clear that the wall of the hollow particles consists of a single layer of NPs with a diameter of ~10 nm. The hollow structure is further confirmed by the TEM image in Figure 32c. The high-resolution TEM (HRTEM) image in Figure 32d clearly shows that the hollow particles were coated with an ultra-thin layer of carbon (~3 nm). The selected area electron diffraction (SAED) image in Figure 32e presents well-defined diffraction rings, indicating that the CuO NPs have a crystalline structure. The crystal nature is confirmed by the X-ray diffraction (XRD) spectrum shown in Figure 32f, which can be indexed to the monoclinic CuO (JCPDS No. 48–1548). The carbon-coated CuO spheres were revealed to contain less than 3 wt% carbon by Thermogravimetric analysis (TGA).
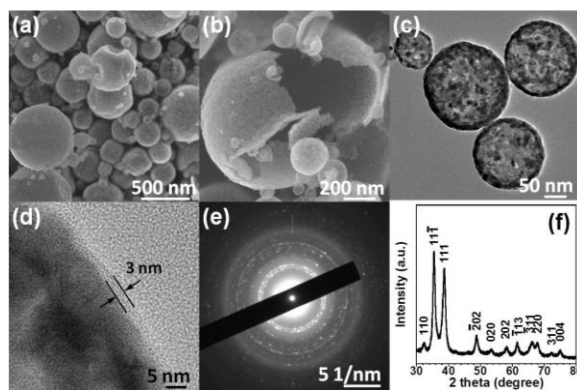
Figure 32. (a,b) SEM, (c,d) TEM, (e) SAED images and (f) XRD spectrum of the nano-structured carbon-coated CuO hollow spherical particles.

The unique structure of the carbon-coated CuO hollow spherical particles enjoys a number of advantages as an anode material in lithium-ion batteries. Firstly, the ultra-small NPs efficiently reduce not only the stress/strain caused by the volume change during the insertion/extraction processes but also the ion diffusion length within the active particles, facilitating the cycling stability and charge transfer reaction. Secondly, void space of the hollow particles is favored to accommodate the large volume change led by chelation reactions. Thirdly, the perfect-assembly single layer structure ensures a large accessible surface area to electrolyte, which enables a fast charge transfer reaction. Fourthly, the thin carbon coating layer provides a mechanical support to maintain the integrity of the CuO NPs upon the repeat cycles. Finally, the thin layer of carbon serves as an electron transportation pathway, enhancing the electric conductivity of the electrode. The functions are illustrated in the schematic figure in Figure 33. Therefore, long cycling stability and good rate capability is anticipated for nano-structured carbon-coated CuO hollow spheres.

The electrochemical performance of the carbon-coated CuO hollow spheres was investigated in coin cells using lithium metal as a counter, and 1 M $LiPF_6$ in a mixture of ethylene carbonate/diethyl carbonate (EC/DEC, 1:1 by volume) as electrolyte. Results are presented in Figure 34. Figure 34a shows the cyclic voltammograms (CV) curves in the initial 5 cycles at a scan rate of 0.1 mV/s between 0 and 3 V. In the first cathodic scan, three peaks were observed at 1.90, 1.12, and 0.88 V, corresponding to the formation of a solid solution of $Cu^{II}_{1-x}Cu^{I}_xO_{1-x/2}$, a phase transition into Cu_2O, and the formation of Cu nanograins dispersed into a lithia matrix (Li_2O), respectively. In the following scans, the 1.12 and 1.90 V peaks shift to and maintained at

47

higher potentials of 1.20 and 2.20 V, respectively. The current peak shift to more positive potential in the second cycle is a common phenomenon for metal oxide anodes and was attributed to the structure changes during the lithium ion insertion in the first lithiation. The higher peak current in the first lithiation was partially attributed to the formation of solid-electrolyte interface (SEI) films. There is no obvious difference in the anodic scans for the first five cycles. The almost identical lithiation/delithiation behaviour from the second cycle demonstrates good reversibility and stability of the carbon-coated CuO hollow spheres.
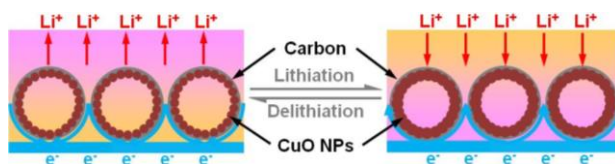

Figure 34. Schematic illustration of structure change during the charge/discharge processes of the nano-structured carbon-coated CuO hollow spherical particles.

4.7.2 Electrochemical performance

Figure 35b shows the charge/discharge profiles of the carbon-coated CuO hollow spheres in the first 5 cycles. It provides a lithiation capacity of 1003 mAh/g and a reversible capacity of 551 mAh/g, corresponding to a Coulombic efficiency of 55%. The irreversible capacity is mainly associated with the formation of SEI films. In the following cycles, capacity slightly increases and the Coulombic efficiency is approaching 100%, showing a good cycling performance.

The cycling performance of the carbon-coated CuO hollow spheres was examined by repeated charge/discharge processes between 0 and 3.0 V at a 1 C rate (670 mA/g). For comparison, commercial CuO NPs with an average particle size of 50 nm were also examined at the same conditions. Data are shown in Figure 35c. The carbon-coated CuO hollow spheres provide a delithiation capacity of 550 mAh/g in the first cycle. After a slight capacity increase for 5 cycles, it becomes stable at ~ 640 mAh/g. Even after 300 cycles, no capacity decay occurred. This is much better than those reports on CuO anodes in literature. The commercial CuO NPs delivered the similar capacity to the carbon-coated CuO hollow spheres in the initial few cycles, but suffered rapid capacity decay to ~450 mAh/g after 50 cycles. These results clearly demonstrate that the superior cycling performance of the nano-structured carbon-coated CuO hollow spheres over the commercial NPs.

The rate capability of the nano-structured carbon-coated CuO hollow spheres and the commercial NPs was investigated by charging (delithiation) at 0.1 C and discharging (lithiation) at different C rates (Figure 35d). The nano-structured carbon-coated CuO hollow spheres demonstrated excellent discharge rate capability. At 20 C, the discharge capacity retention is about 580 mAh/g. Even at very high rate of 50 C (3.35 A/g), it still retained as high as 400 mAh/g, which means the carbon-coated CuO hollow sphere anodes can be discharged in 1.2 minutes with higher capacity retention than graphite anodes. Up to date, this is the best rate performance for CuO anodes. In contrast, the commercial NPs failed to provide capacity at 20 C. The excellent discharge capability of the nano-structured carbon-coated CuO hollow spheres demonstrated a significant advance in Li-ion battery technologies because the discharge power density is critical for most practical applications. The exceptional electrochemical performance is attributed to the unique structure of the nano-structured carbon-coated hollow particles.
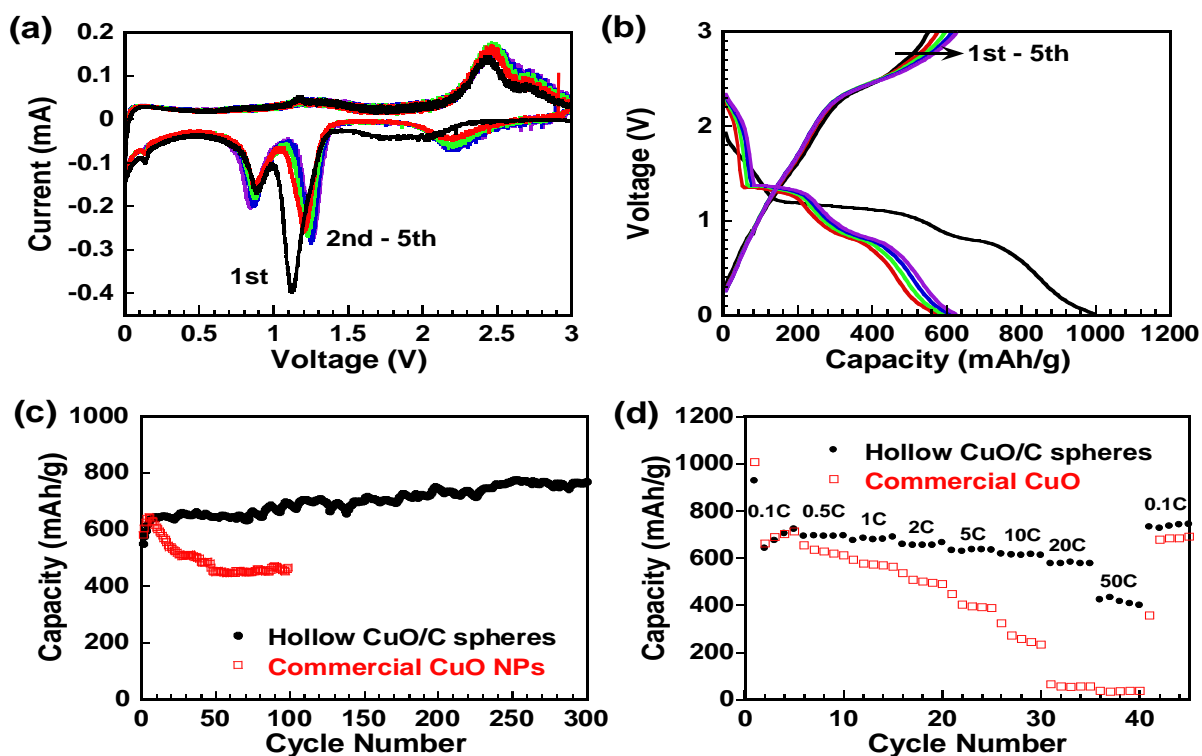

Figure 35. Electrochemical performance of the nano-structured carbon-coated CuO hollow spherical particles and commercial CuO NPs. (a) CV curves, (b) charge/discharge profiles, (c) cycling stability, and (d) rate capability.

The morphology changes of the nano-structured carbon-coated CuO hollow particles after 70 charge/discharge cycles between 0 and 3.0 V at 1 C were investigated using SEM (Figure 36). It

is shown in Figure 4a that most hollow CuO particles preserved the spherical morphology and the architecture of the as prepared samples (shown in Figure 1). It was found some particles collapsed due to either mixing/coating process or repeated charge/discharge cycles, but the integrity of the single layer CuO NPs was kept in a sheet structure (Figure 4c). The robust structure ability is believed to be associated with the carbon coating layer, which provides both mechanical support and electric pathway, thus ensuring good cycling stability and fast rate capability.
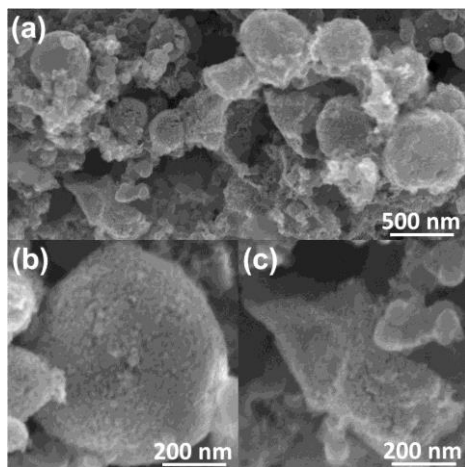

Figure 36. SEM images of the nano-structured carbon-coated CuO hollow spherical particles after 70 charge/discharge cycles.

5. Conclusions

Three kinds of Si/C composite and one porous iron oxide anode materials were synthesized and characterized for lithium ion. All these anodes materials show promising electrochemical performance. First, the self-assembled microsized porous Si/C particles synthesized by electrospray delivered a high reversible capacity of over 2000 mAh/g and a high efficiency of 82% in the first cycle. The unique structure, including that the porous structure offers addition space to accommodate the volume change caused by the lithium ion insertion/extraction, and the uniform distributed carbon in the microparticles provides mechanical support to release the stress during cycling. Second, the yolk-shell structured Si anodes were prepared using an in-situ polymerization and chemical etching method. The yolk-shell structured Si anodes showed enhanced cycling stability. There is no capacity fading over 30 cycles. The superior stability is attributed to the void feature of the yolk-shell structure, which can effectively digest the volume expansion upon lithiation reaction. Third, uniform carbon-coated Si was synthesized by in-situ

polymerization on the surface of Si particles. The super stable cycling performance was obtained with 98% capacity retention over 100 cycles. The uniform carbon coating is believed to be responsible for the good stability. Forth, mesoporous Fe_2O_3 spherical particles were synthesized at different temperatures of 600 C and 800 C using aerosol spray pyrolysis. High capacity, good cycling stability as well as excellent rate capability were demonstrated for Fe_2O_3-800. It is also found that the crystalline Fe_2O_3 better electrochemical performance than amorphous Fe_2O_3, which suggests that crystal structure is preferred for high performance Fe_2O_3 anode materials in LIBs. Finally, Carbon-coated CuO hollow spheres with a single layer of CuO nanoparticles anchored to the outside carbon layer were also synthesized using the aerosol spray pyrolysis method. The hollow spherical particles provide capacity of 670 mA/g at 1C and maintain the capacity to 300 cycles and retain capacity of 400 mAh/g at 50 C. This is the best performance for CuO anodes reported up to date. Our study not only provides a simple synthesis method for lithium ion batteries, but also helps in designing novel and high performance electrode materials.

In additional to anode materials, mesoporous carbon/sulfur composite was synthesized using vacuum vapor infusion method as cathode material for sodium-ion and lithium-ion batteries. The stability of sulfur was revealed by in-situ TEM beam irradiation and electrochemical cycling test for Na-S and Li-S batteries. For Na-S cells, after 300 cycles, the capacity retention is still as high as 712 mAh/g. This is the first time that long cycle life room temperature Na-S batteries were successfully built. For Li-S batteries, The influence of existing form of sulfur and electrolytes was investigated. the interior sulfur inside the porous carbon was not influenced by the choice of electrolytes, and show stable cycling stability. This design of porous carbon-trapped small suflur molecules essentially avoids the formation of soluble polysulfides intermediates and excludes the shuttling effects, thus enhancing the electrochemical performance. Perticularly, exceptional cycling performance was demonstrated for S40 with carbonate-based electrolyte, no capacity decay and near 100% Coulombic efficiency over 2050 cycles, which benefits from the unique design and more stable SEI films for carbonate-based electrolytes than ether-based electrolytes. In combination with the nature of low cost, nontoxity and wide availability over the world of sulfur, the good electrochemical performance makes the mesoporous C/S composite extremely promising cathode materials for the large-scale energy storage.